MORB differentiation: *in situ* crystallization in replenished-tapped magma chambers

[1*]L.A. Coogan, and [2#]M.J. O'Hara

[1]School of Earth and Ocean Sciences, University of Victoria, Victoria, BC, Canada, V8P 5C2; Tel: (1) 250 472 4018; Fax: (1) 250 721 6200; lacoogan@uvic.ca

*corresponding author

[2]Institute of Geography and Earth Sciences, Aberystwyth University, Aberysthwyth SY23 3DB, UK, #deceased

Revised version returned 2nd March 2015

16

17 **ABSTRACT**

18 The differentiation of mid-ocean ridge basalt (MORB) is investigated with a focus on
19 intermediate- to fast-spreading ridges and two recently proposed differentiation
20 mechanisms: (i) differentiation in replenished-tapped crystallizing (RTX) magma
21 chambers, and (ii) chromatographic element separation during melt-rock reaction in the
22 lower crust. There is compelling evidence in the petrology and geochemistry of MORB
23 indicating that magma chambers at mid-ocean ridges behave as open systems, as required
24 on thermal grounds in locations where a steady-state magma chamber exists. It has
25 recently been suggested that the commonly observed over-enrichment of more-to-less
26 incompatible elements during MORB differentiation can be explained by such an RTX
27 model. However, the petrology of samples from the lower oceanic crust suggests an
28 alternative mechanism could produce this over-enrichment. Clinopyroxene crystals in
29 oceanic gabbros are commonly strongly zoned in incompatible elements with crystal rims
30 apparently having grown from melts with very high incompatible element abundances.
31 Elevated Zr/LREE in clinopyroxene rims, which has been interpreted as indicating
32 growth from a melt in which these elements had been fractionated from one another by
33 melt-rock reaction (chromatographic separation), is shown to be more simply explained
34 by post-crystallization diffusive fractionation. However, the high incompatible element
35 abundances in crystal rims demonstrates that the interstitial melt in crystal mush zones
36 becomes highly differentiated. Disaggregation of such mush zones is indicated by the
37 crystal cargo of MORB and must be accompanied by the return of interstitial melt to the
38 eruptible reservoir – a form of *in situ* crystallization. Both a magma chamber undergoing

closed system *in situ* crystallization, and a RTX magma chamber in which crystallization occurs *in situ*, are shown to be capable of reproducing the differentiation trends observed in MORB. Simple stochastic models of the latter process suggest that significant variations of incompatible element abundances and ratios, at a constant MgO content, are likely to be generated from a single parental melt compositions. Additionally, parental melt compositions will generally be substantially more depleted than would be suggested if only fractional crystallization is considered. This has important implications for understanding the composition of the upper mantle. For example, the Sm/Nd of MORB are likely to be significantly lower than that of the Moho-crossing melt complicating analysis of the Nd-isotopic evolution of the upper mantle.

Keywords: differentiation, gabbro, magma chamber, MORB

1. INTRODUCTION

The compositions of mid-ocean ridge basalts (MORB) provide a window into the composition and temperature of the upper mantle. However, it has long been known that MORB compositions are more evolved (e.g., lower Mg# = Mg/(Mg+Fe) in molar units) than primary mantle melts and that they have compositions close to low-pressure cotectics. This demonstrates that erupted melt compositions are strongly influenced by low-pressure crystallization (e.g., O'Hara, 1968). However, low-pressure differentiation has generally been thought to play a minor role in changing the ratios of incompatible elements in MORB; this is largely because incompatible elements are difficult to fractionate from one another during perfect fractional crystallization. The favoured place to produce variations in incompatible element ratios has generally been in the mantle, either due to differences in melting (extent, process, etc) or mantle composition. This is despite several early studies noting that apparently co-genetic suites of MORB show evidence that partial crystallization can fractionate incompatible elements in ways not expected during perfect fractional crystallization (Bryan et al., 1976; White and Bryan, 1977; Perfit et al., 1983, Hekinian and Walker, 1987).

Recently, O'Neill and Jenner (2012) reopened the debate about whether incompatible element abundances and ratios in MORB provide a transparent window into the mantle or are significantly modified by differentiation processes. Using a global dataset of MORB major and trace element compositions (Jenner and O'Neill, 2012) they demonstrated that with decreasing MgO content there is more enrichment in incompatible element abundances than can be achieved by fractional crystallization. The extent of

enrichment of incompatible elements correlates with the elements bulk partition coefficient meaning that more-to-less incompatible element ratios increase with differentiation. They propose that a series of steady-state replenished-tapped-crystallizing (RTX) magma chambers along the global ridge system can explain these observations. However, this model requires a specific relationship between the mass fractions of melt crystallized in, and tapped from, the steady-state magma chamber with both of these decreasing with decreasing melt MgO content (their Fig. 4b; see Section 3).

Plutonic rocks from the lower oceanic crust are the crystallization products of MORB differentiation and hence provide important insights into the processes involved in driving compositional variations in erupted basalts (e.g. Coogan, 2014). Relative to the upper crust, lower crustal rocks are strongly depleted in incompatible elements. Moreover, the extent of depletion correlates with both the elements bulk partition coefficient, and with the variability of the element in the overlying upper crust (Coogan et al., 2001). For example, La is roughly twice as enriched in the upper crust relative to the lower crust compare to Lu (Coogan, 2014). However, the concentration of incompatible elements in plutonic rocks is strongly influenced by any "trapped melt" (Barnes, 1986), complicating the use of whole-rock compositions of plutonic rocks in understanding MORB differentiation.

In part because of the problems associated with "trapped melt", the compositions of minerals in plutonic rocks have generally been thought to be more informative about differentiation processes than bulk-rock analyses. The basic premise is that spot analyses of minerals can be used to directly calculate parental melt compositions by dividing by an appropriate partition coefficient. Trace element analyses of clinopyroxene in oceanic

gabbros show strong fraction of more-to-less incompatible elements both from core-to-rim within individual crystals and within regional and global datasets (Ross and Elthon, 1997; Coogan et al., 2000a; Gao et al., 2007; Drouin et al., 2009; Lissenberg et al., 2013). Incompatible element abundances can vary by an order of magnitude from core-to-rim within a clinopyroxene crystal despite major and compatible minor elements showing little variation. Most striking is the substantial fractionation of Zr from the LREE's that has been interpreted to indicate that within the crystal mush Zr behaves significantly more incompatibly than the LREE. Based on the assumption that the clinopyroxene compositions record growth from melts with equally variable trace element compositions, the observed fractionation of Zr from LREE's has been suggested to be generated by porous melt migration and melt-rock reaction (Coogan et al., 2000a; Gao et al., 2007; Lissenberg et al., 2013). Return of such differentiated interstitial melt to an eruptible reservoir could lead to substantial fractionation of incompatible element ratios in the mixed magma. This has been proposed as an alternative mechanism to explain the over-enrichment of incompatible elements in MORB (Lissenberg et al., 2013; Coogan, 2014). However, the use of mineral compositions to track melt differentiation relies on the largely untested assumption that elements are immobile after crystal growth (Coogan, 2014).

Here the differentiation of MORB is reconsidered. After recapping some key observational constraints on MORB differentiation (Section 2) the RTF model of O'Neill and Jenner (2012) is re-examined with a focus on intermediate- to fast-spreading ridges where steady-state magma chambers are common (Section 3). The use of the compositions of mineral in oceanic gabbros to determine their parental melt compositions

is considered in Section 4 and it is demonstrated that post-crystallization diffusion modifies mineral compositions preventing simple determination of their parental melt compositions. Thus, models of melt-rock reaction in a crystal mush, based on mineral trace element compositions, need reconsidering. That said, there is unambiguous evidence that interstitial melts become highly enriched in incompatible elements and return of this melt to an eruptible reservoir (*in situ* crystallization) is hence examined (Section 5). *In situ* crystallization in a magma chamber undergoing replenishment and tapping is able to explain the global incompatible trace element over-enrichment observed in the MORB dataset of Jenner and O'Neill (2012) and the range of compositions in a broadly cogenetic suite of MORB and plutonic rocks from Hess Deep. We conclude that *in situ* crystallization in a magma chamber undergoing replenishment and tapping is consistent with the geochemistry and petrology of the oceanic crust, as well as thermal constraints. This has important implications for the interpretation of MORB in terms of mantle processes and composition (Section 6).

2. OBSERVATIONAL CONSTRAINTS ON MORB DIFFERENTIATION

Models for the differentiation of MORB, and crystallization of the plutonic section of the oceanic lithosphere, must explain how a primitive parental melt composition differentiates to produce more fractionated magmas. The simplest model to compare observed MORB compositions to is perfect fractional crystallization in a closed system. Studies of MORB differentiation have identified four key features of the differentiation trends that are inconsistent with closed system fractional crystallization being the sole differentiation process and that any successful model of MORB differentiation must be able to explain.

144 Firstly, the relative increase in the abundance of highly incompatible elements
145 with differentiation is commonly greater than can be explained by fractional
146 crystallization (e.g., Fig. 1a). This was demonstrated many years ago for both a global
147 dataset of MORB (Bryan et al., 1976) and well-studied samples from specific locations,
148 some of which have been shown to be nearly isotopically homogeneous, such as the
149 FAMOUS area (Bryan et al., 1977; White and Bryan, 1977), the Galapagos area (Perfit et
150 al., 1983) and 21°N on the East Pacific Rise (EPR; Hekinian and Walker, 1987). Both
151 crystallization (e.g., O'Hara, 1977; Langmuir, 1989) and mantle melting (e.g., Frey et al.,
152 1993) processes have been used to explain such data. These observations have recently
153 been re-emphasized with a greatly expanded dataset (O'Neill and Jenner, 2012). It is
154 important to note that all authors agree that parental melt heterogeneity is also required
155 (e.g., Bryan et al., 1976; O'Neill and Jenner, 2012).
156 Secondly, the depletion of the highly compatible elements is commonly much less
157 than is predicted by perfect fractional crystallization (Fig. 1b; e.g., O'Hara and Fry,
158 1996a,b). This observation is less readily quantified than the over-enrichment of
159 incompatible elements because the bulk partition coefficients for the highly compatible
160 elements (largely Ni and Cr in most datasets) are more uncertain and vary with
161 crystallizing assemblage and temperature. However, the large range of Ni (and Cr)
162 contents in moderately evolved basalts are difficult to explain if differentiation occurs
163 solely by perfect fractional crystallization (Fig. 1b).
164 Thirdly, for a single suite of MORB the mineral assemblage extract required to
165 drive the differentiation of the more primitive compositions to produce the more evolved
166 compositions is commonly inconsistent with the observed 'phenocryst' assemblage

and/or the phase assemblage that the melt is saturated with. The most well-known example of this is the so-called "pyroxene paradox" in which in some locations modeling shows that clinopyroxene must be part of the bulk crystal extract that generates more evolved lava compositions from more primitive one (e.g., due to decreasing or constant Ca/Al with decreasing MgO) but clinopyroxene is commonly neither observed as a phenocryst phase nor is on the liquidus of all of the more evolved lavas (e.g., Bryan et al., 1976; Dungan and Rhodes, 1978). This can be seen in the Smithsonian global MORB glass database, in which the average Ca/Al of MORB stays approximately constant during differentiation (Fig. 1c). Least squares modeling of the cumulate extract required to drive the changes in MORB composition (e.g., Bryan et al., 1969) shows that clinopyroxene is required to be part of the crystallizing assemblage even in the most primitive compositions. Likewise, primitive MORB that only have olivine on their liquidus have been shown to have negative Eu anomalies suggestive of plagioclase fractionation (Rhodes et al., 1979).

Finally, the 'phenocryst' assemblage in MORB is commonly not in equilibrium with the lava they are hosted in – i.e., the crystal cargo of most MORB are not true phenocrysts. This can be determined texturally (e.g., Dungan and Rhodes, 1978) and/or compositionally; most olivine and plagioclase crystals in MORB are more primitive than those in equilibrium with the host basalt (Fig. 1d; Bryan and Moore, 1977; Rhodes et al., 1979; Pan and Batiza, 2003; Coogan, 2014). In many cases it can be shown that mixing occurred within weeks to months before eruption (e.g., Pan and Batiza, 2002; Costa et al., 2009; Moore et al., 2014). Additionally, glomerophyric clusters of crystals, and small plutonic xenoliths containing interstitial melt, are found in some MORB suites (e.g.,

Hekinian et al., 1985; Ridley et al., 2006) suggesting disruption of mush zones accompanies eruption in some instances; this provides a mechanimsm for interstitial melt to be returned to an eruptible melt reservoir.

In addition to these four features, chlorine is commonly substantially over-enriched with respect to other similarly incompatible elements in evolved MORB from fast- but not slow-spreading ridges (Michael and Schilling, 1989; Michael and Cornell, 1998). This suggests assimilation of country rock that had interacted with seawater (Michael and Schilling, 1989; Michael and Cornell, 1998). However, whether small amounts of Cl-rich material (brine; e.g., Michael and Schilling, 1989), or large amounts of Cl-poor material (altered rock; e.g., Coogan et al., 2003), is assimilated is debated and, for simplicity, assimilation is not considered further here; this will need including in any comprehensive model of MORB differentiation.

3. REPLENISHED-TAPPED MAGMA CHAMBERS

At intermediate- to fast-spreading mid-ocean ridges geophysical studies have shown that much of the ridge axis is underlain by a melt lens or sill near the base of the sheeted dike complex (the axial magma lens or AML; e.g., Detrick et al., 1987; Kent et al., 1993). Preventing such a body freezing requires replenishment on a decadal timescale (Phipps Morgan and Chen, 1993; Liu and Lowell, 2009; Moore et al., 2014) similar to the average timescale for dike emplacement. This physical constraint appears robust and hence replenished-tapped magma chambers must be common at intermediate- to fast-spreading mid-ocean ridges.

O'Neill and Jenner (2012) recently re-invigorated the idea that an open system magma chamber undergoing replenishment and tapping could lead to the over-

enrichment of incompatible elements in MORB that has been widely documented (Fig. 1a). The basic premise behind this model is that, at steady-state, the replenishing material must match the crystallized and erupted material both in mass and composition. Different forms of this model exist depending on two main variables: (i) the crystallization process in the magma chamber (e.g., equilibrium, fractional, *in situ* crystallization, etc); and (ii) the relative orders of replenishment (R; potentially including assimilation), mixing (M), crystallization (X) and tapping (T). O'Hara (1977) introduced the equations for the steady-state open system model assuming the sequence RTMX and Albarède (1985) introduced the equations (subsequently reformulated by O'Hara and Herzberg, 2002) for the sequence RMTX.

O'Neill and Jenner (2012) used Albarède's (1985) equations to explain the global variation in over-enrichment of incompatible trace elements with decreasing MgO relative to fractional crystallization that they observed (e.g., Fig. 1a). They suggested that to explain the data with this model, a systematic relationship between the mass fractions of the steady-state magma chamber that are crystallized (x) and tapped (y) must exist. O'Neill and Jenner (2012) took the novel approach of determining the values of x and y required to produce a melt with any given MgO content from the covariation of those elements that appear to behave perfectly incompatibly. The most highly incompatible elements Th, Rb, Cs, Ba, Nb and Ta all have the same slope on plots of Log[X] v MgO and O'Neill and Jenner (2012) interpret this as indicating that they all share a partition coefficient of zero. Given this, and the bulk partition coefficient for MgO ( ), the values of x and y required to fit this slope at any given MgO content are fixed (Fig. 4b in O'Neill and Jenner, 2012). Unfortunately, the Albarède (1985) formulation is not

236 constrained so that the mass fraction crystallized and the mass fraction tapped cannot
237 exceed unity; this means that the bounds on the steady-state region in Fig. 4 of O'Neill
238 and Jenner (2012) are incorrect. A correct equation for a RMTX magma chamber
239 composition is presented by O'Hara and Herzberg (2002). Figure 2a reproduces the
240 RMTX modeling of Fig. 4b of O'Neill and Jenner (2012) but using the O'Hara and
241 Herzberg (2002) equations. This is similar to that of O'Neill and Jenner (2012), except at
242 high MgO contents which are achievable at steady-state, and thus their main conclusions
243 are unaffected.

244 Because analytical solutions to the RMTX models only exist under the
245 assumption of constant partition coefficients, the approach described above is a
246 simplification using a fixed value for [ ] as well as for trace elements. As discussed by
247 Nielsen (1988; 1990), bulk partition coefficients in replenished-tapped magma chambers
248 will depend on the mass fractions replenished, tapped and crystallized due to phase
249 equilibria constraints. In this study constant trace element partition coefficients are
250 assumed throughout to make the results transparent. However, since O'Neill and Jenner
251 (2012) used MgO as an indicator of the extent of differentiation the effect of varyiable
252 [ ], and treating major element differentiation robustly, is investigates using a series of
253 Petrolog (Danyushevsky and Plechov, 2011) models to simulate RMTX. The initial melt
254 was allowed to crystallize a given amount and then the resulting melt composition was
255 mixed back with the initial composition (simulating replenishment) and the process
256 repeated.

257 The steady-state melt MgO content produced by the Petrolog model is broadly
258 similar to that determined using [ ] = 1.9, as used by O'Neill and Jenner (2012; Fig.

2b). The models shown in Figure 2b were not iterated enough times to reach the steady-state K_2O content (K behaves perfectly incompatibly in this modeling and thus can be treated analytically), but the MgO content reached near-steady-state changing by <0.02 wt% per cycle. The constant $\square = 1.9$ approximation somewhat over-estimates the steady-state MgO content in this modeling, especially at high steady-state MgO contents, but only by a small amount. The inset in Figure 2b shows that under some conditions a very large number of cycles of replenishment, tapping and crystallization are required for perfectly incompatible elements to reach the steady-state composition. For example, roughly 100 cycles are required to reach steady-state for the (realistic) case of 4% tapped and 16% crystallized per cycle (Fig. 2b inset). Thus, only at ridges with long-lived magma chambers are the maximum incompatible element abundances, of the steady-state magma chamber, likely to be achieved.

An important feature of open system magma chambers, discussed by Nielsen (1990) and clearly demonstrated by the Petrolog modeling, is that the behaviour of elements that have highly non-linear differentiation paths, due to changes in the crystallizing assemblage and hence bulk partition coefficients, can be complex. This is demonstrated for CaO-MgO in a RMTX magma chamber (Fig. 2c). As the mass fraction crystallized per cycle increases, the residual melt *before* replenishment becomes more depleted in both MgO and CaO; in turn the larger mass fraction crystallized requires a larger mass fraction of replenishing magma to maintain the magma chamber mass (assuming a fixed mass fraction tapped). This leads to a higher melt MgO content at a given CaO content in the erupted (*mixed*) magma in the RMTX model. The variation in differentiation paths shown in Fig. 2c for models with different mass fraction tapped and

crystallized per cycle are similar to those that have been interpreted as indicating variable pressures of differentiation, questioning whether such interpretations are valid. For example, the near-steady-state compositions shown in Fig. 2c give pressures of 1.4, 3.8 and 5.8 kbars when processed through the Villiger et al. (2007) melt barometer despite all models being run at 1 kbar.

4. INTERSTITIAL MELT DIFFERENTIATION

Despite compelling evidence that mid-ocean ridge magma chambers are open systems (Section 3), the mechanism of crystal-melt separation is also important in controlling the differentiation path followed – oceanic plutonic rocks potential provide important insight into this. Clinopyroxene crystals in oceanic gabbros commonly show strong zoning of incompatible elements (Ross and Elthon, 1997; Coogan et al., 2000a; Gao et al., 2007; Lissenberg et al., 2013) suggesting that the interstitial melt that the rims of these crystals grew from was enriched in incompatible elements (Fig. 3a). Return of such interstitial melt to an eruptible magma reservoir (i.e., a form of *in situ* crystallization; Langmuir, 1989) could be important in controlling MORB differentiation. Perhaps the most striking feature of the trace element enrichment in the clinopyroxene rims is the substantial over-enrichment of Zr with respect to the LREE (Fig. 3a; Coogan et al., 2000a; Gao et al., 2007; Lissenberg et al., 2013). This enrichment cannot be explained by closed system fractional crystallization of interstitial melt (Coogan et al., 2000a) and has been interpreted to indicate melt-rock reaction during migration of an interstitial melt through a crystal mush (Coogan et al., 2000a; Gao et al., 2007; Lissenberg et al., 2013). Return of interstitial melt, that has differentiated via melt-rock

304 reaction, to an eruptible reservoir has been proposed to play an important role in MORB
305 differentiation (Lissenberg et al., 2013).

306 Given the large increases in Zr/LREE in the rims of many clinopyroxene crystals
307 in oceanic gabbros, a striking feature of the Jenner and O'Neill (2012) MORB database is
308 that there is no such over-enrichment of Zr with respect to LREE in MORB; instead, Nd
309 and Zr have identical slopes on plots of MgO v Log[X]. The same is true in the MORB
310 database of Gale et al. (2013; inset Fig. 3a). Thus, if the over-enrichment of Zr observed
311 in clinopyroxene rims is due to crystallization from an interstitial melt over-enriched in
312 Zr with respect to Nd, then return of this interstitial melt to the eruptible reservoir plays
313 little or no role in MORB differentiation. However, before discounting the return of
314 interstitial melt to an eruptible reservoir we reconsider the melt-rock reaction model for
315 producing the high Zr/LREE in clinopyroxene rims in light of trace element diffusion
316 coefficients for clinopyroxene and plagioclase (Van Orman et al., 2001; Cherniak, 2003)
317 that have been published since this model was first proposed.

318 To investigate whether magmatic trace element zoning could be modified by
319 diffusion during cooling of an oceanic gabbro a simple numerical model of this process
320 was constructed as follows. A plane sheet geometry was assumed with a 1 mm diameter
321 clinopyroxene adjacent to a 2 mm diameter plagioclase. Arrhenius relationships for the
322 diffusion coefficients of REE's were taken from Van Orman et al. (2001) for
323 clinopyroxene and Cherniak (2003) for plagioclase (Supplementary material Appendix
324 1); the latter are about one order of magnitude larger for the HREE and two orders of
325 magnitude larger for the LREE's at magmatic temperatures. Temperature-dependent
326 partition coefficients for the REE's between plagioclase and clinopyroxene were

determined using the crystal-melt partition coefficients of Wood and Blundy (2003) with the subsolidus relationship derived by taking the ratio of the crystal-melt partition coefficients (i.e., $kd_{plag/melt}/kd_{cpx/melt} = kd_{plag/cpx}$; Supplementary material Appendix 1). The initial concentration profiles were set assuming closed system fractional crystallization (using the same partition coefficients), producing strongly zoned crystals with incompatible element enriched rims (Fig. 4). Diffusion was modeled from an initial temperature of 1200°C down to 700°C (below which diffusion is too slow to modify REE distributions significantly) at cooling rates of $1x10^3$ and $5x10^3$ °C Myr^{-1} appropriate for much of the lower oceanic crust (John et al., 2004; Coogan et al., 2007).

While the models shown in Figure 4 are for one specific texture, and should not be expected to match all natural samples, the overall behaviour appears to explain many observations from natural samples. Perhaps most importantly the models show that subsolidus modification of REE (and Y) distributions is likely in the lower oceanic crust (and many mafic plutons) and must be considered when interpreting intra-crystal compositional variations (the same is true for Nd- and Sr-isotopes). The behaviour of an element depends on both its partition and diffusion coefficients.

Lanthanum diffuses much more rapidly in plagioclase than in clinopyroxene and has a slightly higher partition coefficient for plagioclase than clinopyroxene at magmatic temperatures, and there is a small increase in [ ] during cooling. The higher diffusivity of La in plagioclase than clinopyroxene means that during cooling the plagioclase tends to homogenize its La content much more rapidly than the clinopyroxene. In turn, due to the assumed equilibrium between plagioclase and clinopyroxene at the grain boundary, there is a flux of La into plagioclase from

clinopyroxene leading to an increase in the bulk La content of plagioclase (Fig. 4a, b). Furthermore, during cooling [ ] increases providing a continued driving force for a flux of La from clinopyroxene into plagioclase.

Ytterbium is used as an example of the HREEs (Fig. 4e, f), but is compared to measured Y concentrations (Fig. 3) because the higher abundances of the latter leads to smaller analytical uncertainties in plagioclase compositions (and diffusion coefficients for Y are not available). As with La, the higher diffusivity of Yb in plagioclase than clinopyroxene means that during the initial stages of cooling the plagioclase tends to homogenize its Yb content much more rapidly than the clinopyroxene. Again, due to the assumed equilibrium between plagioclase and clinopyroxene at the grain boundary there is a flux of Yb into plagioclase from clinopyroxene leading to an overall enrichment in the concentration of Yb in plagioclase. This behaviour is somewhat counter-intuitive because during cooling [ ] decreases driving Yb from plagioclase to clinopyroxene. These counteracting driving forces lead to potentially quite complex behaviour. For sufficiently slow cooling rates the change in [ ] with temperature will lead to plagioclase with Yb depleted rims (Fig. 4f). The flux of HREE's from plagioclase into clinopyroxene will have little effect on the clinopyroxene composition due to the low abundance of these elements in plagioclase compared to clinopyroxene. The distribution of HREE and Y appear to have the potential to provide quantitative information about cooling rates in such rocks.

In combination the behaviour of La and Yb (or Y) in plagioclase may be diagnostic of diffusive modification of REE distributions. All REE's (and Y) are incompatible in the main phases found in oceanic cumulates (olivine, plagioclase,

pyroxenes, FeTi oxides) and hence crystal-melt separation at decreasing melt mass will tend to enrich these elements in the later crystallization products. Thus, in general, one would expect crystal rims to be relatively REE enriched over crystal cores. This is generally the case for La in plagioclase with rim-to-core ratios >1 in most crystals (Fig. 3c). In contrast, Y is commonly depleted in plagioclase rims compared to their cores (Fig. 3b and c). This led both Coogan et al. (2000b) and Lissenberg et al. (2013) to suggest that different parental melts had to be involved. Instead, it appears that the high mobility of REEs in plagioclase (Cherniak, 2003) leads to post-crystallization diffusive loss of Y from plagioclase into clinopyroxene (Fig. 4f).

To our knowledge the diffusion coefficient of Zr in clinopyroxene has not been determined experimentally. However it is likely that Zr, a tetravalent cation, will diffuse more slowly than Nd in clinopyroxene tending to fractionate these elements. Further, the partition coefficient for Zr in plagioclase is extremely small meaning that the clinopyroxene acts as an effectively closed system for Zr. This is important because it means that magmatic Zr zoning can only be lost via diffusion of Zr into the clinopyroxene core, and not via loss from the clinopyroxene rim into plagioclase as occurs for the REEs. As a first approximation, the initial profile for Nd (Nd_{ini}) is assumed to match the final Zr profile (i.e., assuming infinitely slow Zr diffusion) and the zoning of Nd_{ini}/Nd is shown as a proxy for Zr/Nd in Fig. 4c (inset). The drop of Nd in the clinopyroxene rim due to the same diffusive fluxes discussed above for La and Yb lead to elevated Nd_{ini}/Nd in clinopyroxene rims and somewhat depleted Nd_{ini}/Nd in clinopyroxene cores. This matches the common observation of sub-chondritic Zr/Nd in clinopyroxene cores and supra-chondrite Zr/Nd in clinopyroxene rims in oceanic gabbros

(Fig. 3a; Coogan et al., 2000a; Gao et al., 2007; Drouin et al., 2009; Lissenberg et al., 2013). Thus, it appears that elevated Zr/LREE in clinopyroxene rims, relative to their cores, in ocean gabbros (or other gabbroic cumulates) does not require melt-rock reaction and chromatographic separation of these elements; instead, this is an expected consequence of slow cooling.

In summary, closed system fractional crystallization of interstitial melt in a crystal mush, followed by subsolidus diffusion, appears to be able to explain the broad variation in trace element compositions in clinopyroxene and plagioclase in oceanic gabbros. While this does not mean that the interstitial melt in the crystal mush evolves via closed system fractional crystallization, there is currently no justification for assuming a more complex crystallization process. However, the high abundance of some incompatible elements, such as La, in both clinopyroxene and plagioclase rims requires that the interstitial melt was highly enriched in incompatible elements. Likewise, the absolute enrichment of Zr in clinopyroxene crystal rims compared to the core of the same crystal cannot be explained by subsolidus processes and must reflect crystallization of the rim from a much more evolved melt than the core. Thus, return of interstitial melt to an eruptible melt reservoir has the potential to lead to substantial enrichment of incompatible elements in erupted MORB. This is evaluated in the following section.

5. REPLENISHED-TAPPED MAGMA CHAMBERS UNDERGOING *IN SITU* CRYSTALLIZATION

The enrichment of La in both plagioclase and clinopyroxene rims (Fig. 3) shows that interstitial melt within crystal mush zones at mid-ocean ridges can become highly fractionated. Evidence for disruption of such crystal mush zones prior to, and during,

eruptions come from the crystal cargo in MORB (e.g., Hekinian et al., 1985; Ridley et al., 2006; Costa et al., 2009; Moore et al., 2014) indicating that evolved interstitial melt must become mixed back into the eruptible magma reservoir. These observations lead us to explore whether *in situ* crystallization (Langmuir, 1989; Nielsen and DeLong, 1992; O'Hara and Fry, 1996b) can explain the observed differentiation trends in MORB. Even though there is clear evidence that mid-ocean ridge magma chambers operate as open systems, we start with a closed system *in situ* crystallization model as this has fewer free parameters and is thus simpler to understand. We then expand this to RMTX magma chambers undergoing *in situ* crystallization – a magma chamber model that appears to be required by the crystal cargo of MORB.

5.1. Closed system *in situ* crystallization

The *in situ* crystallization model (Langmuir, 1989) was developed to explore the geochemical effects of crystallization of melt within a crystal mush boundary layer, followed by return of interstitial melt to an eruptible magma reservoir although the approach can describe other "small packet" crystallization processes (O'Hara and Fry, 1996b). Relative to fractional crystallization, *in situ* crystallization leads to higher abundances of compatible elements at any given mass fraction of crystallization because these elements are only depleted from the melt in the crystallizing boundary layer. In contrast, incompatible elements can become substantially enriched in the residual melt in the mush zone, and fractionated from one another, and return of this interstitial melt to the eruptible reservoir allows fractionation of incompatible element abundances and ratios in erupted melts.

As a staring point the simplest model of Langmuir (1989; Eq. 6) is used to test whether *in situ* crystallization can broadly explain the differentiation trends observed by O'Neill and Jenner (2012). In this the mush zone is assumed to undergo equilibrium partial crystallization to a uniform extent with return of the interstitial melt to the eruptible reservoir after a given extent of crystallization. Bulk partition coefficients are held constant despite the possibility of various phases saturating in the boundary layer; this would lead to variable bulk partition coefficients (Nielsen and DeLong, 1992). Following O'Neill and Jenner (2012), the fit of the model to the data is compared using the slopes of plots of Log[X_i] versus MgO. The slopes of the lines in these plots depend on the relative fractionation of element *i* from MgO during differentiation assuming a constant parental melt composition. The main parameter (other than the partition coefficients) in this modeling that has a strong control on the slope of plots of Log[X_i] versus MgO for realistic ranges of the parameters is *f*, the fraction of melt remaining in the boundary layer at the stage at which interstitial melt is returned to the eruptible reservoir. Variations in the total fraction of melt remaining in the system (F) and the proportion of the interstitial melt that is trapped within the mush (f_T) versus returned to the eruptible reservoir (f_a) largely play off against one another and have a lesser effect on the slope of plots of Log[X_i] versus MgO (Supplementary material Appendix 2). To make the results directly comparable to the model of O'Neill and Jenner (2012) all partition coefficients were taken from their study, and the slope of the model was determined for melt MgO contents between 5.5 to 9 wt%. Trial and error showed that for a value of *f* of 0.4 the *in situ* crystallization model reproduces the general variation observed in the data

(Fig. 5) indicating that *in situ* crystallization is a plausible mechanism for generating the observed over-enrichments in incompatible trace elements observed in MORB (Fig. 1a).

5.2. A replenished-tapped *in situ* crystallization model

To explore a more realistic model we consider a RMTX magma chamber in which crystallization occurs *in situ* (O'Hara and Fry, 1996a, 1996b; O'Hara and Herzberg, 2002). The inputs for this modeling are the relative mass fractions replenished, tapped and crystallized per cycle and the extent and mechanism of crystallization in the boundary layer. The relative mass fractions tapped and crystallized per replenishment cycle are set to 1:4 to approximate the ratio of upper (lava and dike) to lower (plutonic) crust formed at intermediate- to fast-spreading ridges. A rough estimate of the mass of magma in the axial magma lens at a fast-spreading ridge is ~35,000 m^3 per m along axis based on a ~750-1000 m wide by 30-50 m high magma chamber. Comparing this to the average mass required to form a dike that breaches the surface and produces a lava flow (~1500 m^3 per m along axis) leads to an estimate of the replenishing magma mass being ~20% of the magma chamber mass (i.e., 4% of the mass is tapped, and 16% crystallized, per cycle). The simplest crystallization process to envisage in the mush zone is perfect fractional crystallization and this is assumed here – this gives less fractionation of incompatible elements from one another than equilibrium crystallization and is thus a conservative model. We assume melt is returned from a 'boundary layer' in which the melt fraction varies linearly from 0.2 to 1 (i.e. 20% to 100% melt) giving an average extent of crystallization in the boundary layer of 40%. The returned melt is the integrated melt composition across this range of extents of crystallization (O'Hara and Fry, 1996b).

485 At steady-state a replenished-tapped magma chamber will have a fixed
486 composition if all parameters are constant. This is clearly not realistic as MORBs show
487 compositional variability on small time and space scales (steady-state results are shown
488 in Supplementary material Appendix 2). To simulate natural variability we allow the
489 mass fraction replenished to vary about the average value of 0.2±0.05 (1σ) using a
490 Gaussian distribution (truncated at zero). Similar numerical models, but of the RMXT
491 process and with fractional crystallization rather than *in situ* crystallization, have been
492 presented by Robson and Cann (1982), Cox (1988) and Nielsen (1988). Synthetic
493 datasets were generated and the slopes of the model results, on plots of MgO versus
494 Log[*X*] for elements (*X*) with different partition coefficients, are shown in Figure 5.
495 Numerical experiments show no variation in the slope of the data arrays with the size of
496 the standard deviation in the mass fraction replenished – this just changes how much
497 variation of Log[*X*] there is at a given MgO content. The similarity between the model
498 and observed slopes demonstrates that a replenished-tapped-crystallizing magma
499 reservoir, in which crystallization occurs *in situ*, can broadly explain the trace element
500 differentiation trends observed in the global MORB dataset of Jenner and O'Neill (2012).

501 **5.3. Comparison of the RMTX *in situ* crystallization model to a well studied MORB**
502 **suite**

503 It is useful to determine whether the RMTX *in situ* crystallization model can
504 reproduce the general features of a suite of spatially associated MORB as a further test of
505 the plausibility of this model. Using spatially associated samples minimizes the
506 likelihood that variations in parental melt composition will lead to variations in trace
507 element abundances that correlate with MgO. Hess Deep provides one of the best studied

508 sections of fast-spread crust, being one of the few places for which there is a
509 comprehensive dataset for upper crustal (lava and dike) compositions along a timeline
510 (Stewart et al., 2002). Additionally, this area has the best-sampled section of lower crust
511 from a fast-spread ridge allowing, to a first-order, a comparison of the model results with
512 the lower crustal composition. Using the same input parameters described above for the
513 mass fractions replenished and tapped per cycle, but a somewhat smaller extent of
514 crystallization of the boundary layer (from 50% to 100% melt), models were run for a
515 highly incompatible element (Nb) and a moderately incompatible element (TiO_2) using
516 the partition coefficients from O'Neill and Jenner (2012). A parental melt MgO content
517 of 10 wt% was used and the parental melt Ti and Nb contents were iterated to find a
518 visual fit to the data. Figure 6 shows that the co-variation of these elements with MgO in
519 the Hess Deep upper crust is entirely compatible with the predictions of this model.
520 Comparison of the model results and data for the plutonic rocks is also useful. The
521 lower crust at the Hess Deep has a bulk TiO_2 content of 0.46±0.08 wt% (Gillis et al.,
522 2014; Nb data are unavailable). However, the upper gabbros have very high bulk-rock
523 TiO_2 contents (1.15±0.09 wt% TiO_2; Gillis et al., 2014) due to large amounts of trapped
524 melt (Coogan et al., 2002). The RMTX *in situ* crystallization model shown in Figure 6
525 produces an average plutonic rock TiO_2 of 0.33 wt%. An average of 7% trapped melt in
526 the lower crust would explain the difference between the modeled TiO_2 content (0.33
527 wt% TiO_2) and that observed (0.46 wt% TiO_2). Thus, an RMTX magma chamber
528 undergoing *in situ* crystallization appears to be consistent with the compositions of the
529 lower crust as well as the upper crust.

530 The modeling shown in Figure 6 demonstrates both that: (i) significant variations
531 in incompatible element abundances and ratios, at constant MgO content, should be
532 expected to be generated by crustal processes, and (ii) parental melt incompatible element
533 abundances may be far lower than expected if simple differentiation processes are
534 assumed. For example, at a constant MgO content there is a factor of two variation in
535 melt TiO_2, and factor of four variation in melt Nb, in the model shown in Fig. 6.
536 Furthermore, there is little correlation of Nb/Ti with MgO but this ratio varies by a factor
537 of 1.8 at constant MgO. This scatter reflects the different response times of elements of
538 different bulk partition coefficient to changes in the mass fractions tapped and
539 replenished (e.g., Fig. 2b). An even more important feature of this differentiation process
540 is that the model parental melts contain significantly lower Nb (0.7 ppm) and TiO_2 (0.65
541 wt%) than might be expected given standard estimates of the composition of the upper
542 mantle and the average extent of melting. For example, assuming Nb behaves perfectly
543 incompatibly, and the parental melt was generated by 10% melting (e.g. Langmuir et al.,
544 1992), the upper mantle Nb content would be 0.07 ppm substantially lower than most
545 estimates of the Nb content of depleted MORB mantle (e.g. 0.15 to 0.3 ppm; Saal et al.,
546 2002; Workman and Hart, 2005).

547 **6. A VIEW OF MORB DIFFERENTIATION AND BROADER IMPLICATIONS**

548 The AML at intermediate- to fast-spreading ridges is underlain by a zone of
549 mixed crystals and melt that extends to the base of the crust (Sinton and Detrick, 1992;
550 Dunn et al., 2000; Crawford and Webb, 2002) and must also commonly have mush zones
551 at its roof and sides. Within any of these mush zones, if heat extraction allows
552 crystallization to occur, the interstitial melt will become more evolved. Extraction of this

553 interstitial melt into eruptible magma will lead to erupted basalt compositions that show
554 the chemical signatures of *in situ* crystallization. Extraction of interstitial melt into the
555 eruptible reservoir may occur via numerous processes (e.g. compaction, compositional
556 convection) but the crystal cargo of MORB suggests that at least some fraction of the
557 interstitial melt is returned because of mush zone disaggregation associated with
558 replenishment (e.g. Hekinian et al., 1985; Ridley et al., 2006; Moore et al., 2014). In this
559 model, eruptions triggered by replenishment will produce basalts with compositions that
560 are mixtures of the resident melt in the AML, the interstitial melt in the mush zone
561 surrounding the AML and the replenishing melt; the latter may be modified by
562 crystallization prior to or during mixing (e.g., Huppert and Sparks, 1980).

563 **6.1. Backtracking MORB compositions to a fixed melt MgO content**

564 Backtracking an erupted melt composition towards a parental melt composition,
565 for either major or trace elements, is not straightforward if realistic magma chamber
566 processes are considered (e.g., O'Hara and Herzberg, 2002). This is demonstrated in the
567 stochastic differentiation model, with random variation in the mass fraction replenished,
568 shown in Figure 6. As shown in the inset, fluctuations in the input parameters lead to
569 multiple apparent differentiation paths; for each path regression of model TiO_2 content
570 back to a constant MgO content would give the impression of the need for variable
571 parental melt compositions. For example, regression through the three sub-datasets
572 shown in the inset of Fig. 6a lead to TiO_2 contents at 8 wt% MgO of 0.5, 1.3 and 2.1 wt%
573 (compared to an actual model parental melt of 0.65 wt% TiO_2 at 10 wt% MgO). While
574 these three examples were selected to show the range of plausible outcomes, it is clear

575 that simple regression may be misleading both in suggesting variability in parental melt
576 composition when none exists, and in determining what the parental melt composition is.

577 **6.2. Do erupted MORB have the same Sm/Nd as parental MORB?**

578 An example of the importance of quantitatively understanding the differentiation
579 of MORB comes from the use of MORB to estimate the Sm/Nd ratio of the upper mantle.
580 It is important to quantify the upper mantle Sm/Nd ratio to help differentiate between
581 models that explain the non-chondritic $^{142}Nd/^{144}Nd$ ratios of most of the "accessible
582 Earth" (e.g., Boyet and Carlson, 2005) in terms of a "hidden reservoir" versus a non-
583 chondritic bulk Earth composition (e.g., Gale et al., 2013). In either model the "accessible
584 Earth" has a Sm/Nd ~6% higher than chondrites (Jackson and Carlson, 2011). Gale et al.
585 (2013) show that (using their nomenclature) ALL MORB and N-MORB have Sm/Nd
586 ratios of 0.319±0.005 and 0.325±0.0046 respectively. They then make a critical
587 assumption, that the basalt Sm/Nd matches that of the parental mantle melt, and back-
588 calculate an upper mantle Sm/Nd ratio of <0.34 from their ALL MORB composition.
589 This is less depleted than that calculated for the "accessible Earth" based on the observed
590 $^{142}Nd/^{144}Nd$ (0.342-0.352) which is inconsistent with the standard model of the MORB
591 source being the complementary depleted reservoir formed by continental crust extraction
592 (e.g., Hofmann, 1988). However, the calculation of the upper mantle Sm/Nd from MORB
593 compositions described above neglects any change in the Sm/Nd due to partial
594 crystallization in the lower crust.

595 Using the RMTX model shown in Fig. 6, but for Nd and Sm, allows estimation of
596 the difference in the Sm/Nd ratio in the parental melt and the erupted melt given the
597 partition coefficients for these elements. O'Neill and Jenner (2012) estimate [ ] =

598 0.118 and [ ] = 0.179 which would produced a steady-state melt with a Sm/Nd ratio of
599 ~85% of the parental melt. The partition coefficients used by O'Neill and Jenner (2012)
600 for plagioclase are at the low end of the range of plausible values, thus as an alternative
601 we use bulk partition coefficients determined from Wood and Blundy (2003;
602 Supplementary material Appendix 1). Assuming a crystallizing assemblage of 30%
603 clinopyroxene, 50% plagioclase and 20% olivine (kd_{ol} = 0) gives a smaller difference in
604 the partition coefficients between these phases ([ ] = 0.14 and [ ] = 0.16). This
605 results in a steady-state melt with a Sm/Nd ratio of ~95% of the parental melt. In either
606 case the MORB source has a significantly higher Sm/Nd than is calculated without
607 accounting for changes in Sm/Nd due to partial crystallization.

608 A prediction of the model just described is that the Sm/Nd ratio in plutonic rocks
609 of the lower oceanic crust should be higher than in cogenetic MORB. Sampling of the
610 lower crust is very limited at fast-spreading ridges. However, sampling of the upper and
611 lower crust at Pito Deep allows direct comparison of their Sm/Nd ratios. In this location
612 the Sm/Nd of lavas and dikes (0.361 ± 0.001; 1 standard error; Pollock et al. 2009) is
613 substantially lower than that of the plutonics (0.396 ± 0.01; 1 standard error; Perk et al.
614 2007) or the bulk crust (0.377 assuming 15% upper crust and 85% lower crust). The same
615 observation of a higher Sm/Nd of lower crustal than associated upper crustal rocks
616 appears to be true in all locations that lower crustal samples are available from (Coogan,
617 2014). The point here is not to estimate the Sm/Nd of the upper mantle, nor to resolve the
618 origin of the non-chondritic $^{142}Nd/^{144}Nd$ ratios of most terrestrial samples, but simply to
619 demonstrate that ignoring the changes in trace element ratios that can be imparted in
620 magma chambers can have far-reaching implications.

7. CONCLUSIONS

The main conclusions of this study are:

1. Consideration of the petrology and geochemistry of MORB and oceanic gabbros suggests a model for MORB differentiation involving both open system magma chambers and *in situ* crystallization. These processes may be linked through replenishment driving the extraction of interstitial melt from crystal mush zones. Both processes likely play a role in generating the over-enrichment in incompatible elements observed in MORB. Other complexities such as diversity in parental melt compositions (Sims et al., 2002; Coogan et al., 2002; Gillis et al., 2014) and assimilation are likely but have not been considered here.
2. Sub-solidus diffusive modification of trace element distributions in minerals in plutonic rocks may be common (e.g., for REE's in pyroxene) or ubiquitous (e.g., for REE's in plagioclase) and needs considering before these are used to interpret magmatic processes. For example, extreme zoning of Zr/LREE in some clinopyroxene crystals in oceanic gabbros does not require growth from a melt with a very high Zr/LREE ratio but may instead reflect post-crystallization diffusive modification of the clinopyroxene compositions (Fig. 4). If clinopyroxene crystal rims in oceanic gabbros did grow from a melt with an elevated Zr/LREE ratio then the lack of significant variation of Zr/Nd with decreasing MgO in MORB would indicate that such interstitial melts do not play a significant role in MORB differentiation.
3. Simple crystallization models cannot be used to back-track the incompatible element abundances in MORB to determine those of the parental melts (e.g., by

assuming fractional crystallization). This will generally lead to substantial over-estimates of the concentration of incompatible elements. If such estimates are used in calculating upper mantle compositions serious problems may ensue.

4. Incompatible element ratios in MORB cannot be assumed to match those of the parental melt. For example, significant variations in Nb/Ti occurs at constant MgO content in the model shown in Figure 6. Even similarly compatible elements like Sm and Nd are fractionated from one another in RMTX magma chambers undergoing *in situ* crystallization. Thus, the Sm/Nd of sampled MORB cannot be assumed to match that of the parental melts and doing so may led to erroneous conclusions about the evolution of the Nd-isotopic composition of the mantle.

ACKNOWLEDGEMENTS

Correspondence with Hugh O'Neill was helpful in clarify the ideas presented here. Ron Fodor, Roger Nielsen and two anonymous reviewers are thanked for constructive critiques.

REFERENCES

Albarède, F., (1985). Regime and trace-element evolution of open magma chambers. *Nature* **318**, 356–358.

Barnes, S. J. (1986). The effect of trapped liquid crystallization on cumulus mineral compositions in layered intrusions. *Contrib. Mineral. Petrol* **93**, 524–531.

Boyet, M. and Carlson, R. W. (2005). ^{142}Nd evidence for early (>4.53 Ga) Global differentiation of the Silicate Earth. *Science* **309**, 576–581.

665 Bryan, W. B., Finger, L. W. and Chayes, F. (1969). Estimating proportions in
666 petrographic mixing equations by least-squares approximation. *Science* **163**, 926–
667 927.
668 Bryan W. B., Thompson, G. Frey, F.A., and Dickey, J.S. (1976) Inferred geologic
669 settings and differentiation in basalts from the deep-sea drilling project. *J. Geophys.*
670 *Res.* **81**, 4285–4304.
671 Bryan, W. B. and Moore, J. G. (1977). Compositional variations of young basalts in the
672 Mid-Atlantic Ridge rift valley near lat 36°49'N. *Geological Society of America*
673 *Bulletin* **88**, 556–570.
674 Caroff, M., Lagabreille, Y., Spadea, P. and Auzende, J.-M. (1997). Geochemical
675 modelling of non-steady state magma chamber chambers: A case study from an ultra
676 fast spreading ridge, East Pacific Rise, 17-19°S. *Geochimica. Cosmochim. Acta* **61**,
677 4367–4374.
678 Cherniak, D.J., (2003). REE diffusion in feldspar. *Chem. Geol*. **193**, 25–41.
679 Coogan, L.A., (2014). The lower oceanic crust, in: Turekian, K., Holland, H.D. (Eds.),
680 *Treatise on Geochemistry*. Elsevier, 497-541.
681 Coogan, L.A., Saunders, A.D., Kempton, P.D., and Norry, M.J., (2000a). Evidence from
682 oceanic gabbros for porous melt migration within a crystal mush beneath the Mid-
683 Atlantic Ridge. *Geophys. Geochem. Geosys*. **1**, Paper No 2000GC000072.
684 Coogan, L.A., Kempton, P.D., Saunders, A.D., and Norry, M.J., (2000b). Evidence from
685 plagioclase and clinopyroxene major and trace element compositions for melt
686 aggregation within the crust beneath the Mid-Atlantic Ridge. *Earth Planet. Sci. Lett*.
687 **176**, 245–257.

688 Coogan, L.A., MacLeod, C.J., Dick, H.J.B., Edwards, S.J., Kvassnes, A., Natland, J.H.,
689 Robinson, P.T., Thompson, G., and O'Hara, M.J., (2001). Whole-rock geochemistry
690 of gabbros from the Southwest Indian Ridge: constraints on geochemical
691 fractionations between the upper and lower oceanic crust and magma chamber
692 processes at (very) slow-spreading ridges. *Chem. Geol*. **178**, 1–22.
693 Coogan, L.A., Gillis, K.M., MacLeod, C.J., Thompson, G., and Hekinian, R., (2002).
694 Petrology and geochemistry of the lower ocean crust formed at the East Pacific Rise
695 and exposed at Hess Deep: a synthesis and new results. *Geochem. Geophys.*
696 *Geosyst*. Special issue, DOI 10.1029/2001GC000230.
697 Coogan, L.A., Mitchell, N.C., and O'Hara, M.J., (2003). Roof assimilation at fast-
698 spreading ridges: an investigation combining geophysical, geochemical and field
699 evidence. *J. Geophys. Res*. **108**, DOI 10.1029/2001JB001171.
700 Coogan, L.A., Jenkin, G.R.T., and Wilson, R.N., (2007). Contrasting cooling rates in the
701 oceanic lithosphere at fast- and slow-spreading mid-ocean ridges derived from
702 geospeedometry. *J. Petrol*. **48**, 2211–2231.
703 Costa, F., Coogan, L.A., and Chakraborty, S., (2009). The time scales of magma mixing
704 and mingling involving primitive melts and melt-mush interaction at Mid-ocean
705 ridges. *Contrib. to Miner. Petrol*. DOI 10.1007/s00410–009–0432–3.
706 Cox, K. G. (1988). Numerical modelling of a randomized RTF magma chamber: a
707 comparison with continental flood basalt sequences. *J. Petrol.* **29**, 681–697.
708 Crawford W. C. and Webb S. C. (2002) Variation in the distribution of magma in the
709 lower crust and at the Moho beneath the East Pacific Rise at 9°-10°N. *Earth Planet.*
710 *Sci. Lett.* **203**, 117–130.

711 Danyushevsky, L. V, and Plechov, P., (2011). Petrolog3: integrated software for
712 modeling crystallization processes. *Geochem. Geophys. Geosyst*. **12**.
713 Doi:10.1029/2011GC003516
714 Detrick, R.S., Buhl, P., Vera, E., Mutter, J., Orcutt, J., Madsen, J., and Brocher, T.,
715 (1987). Multi-channel seismic imaging of a crustal magma chamber along the East
716 Pacific Rise. *Nature* **326**, 35–41.
717 Drouin, M., Godard, M., Ildefonse, B., Bruguier, O. and Garrido, C. J. (2009).
718 Geochemical and petrographic evidence for magmatic impregnation in the oceanic
719 lithosphere at Atlantis Massif, Mid-Atlantic Ridge (IODP Hole U1309D, 30??N).
720 *Chemical Geology* **264**, 71–88.
721 Dungan, M.A. and Rhodes, J.M., (1978). Residual glasses and melt inclusions in basalts
722 from DSDP Legs 45 and 46: evidence for magma mixing. *Contrib. Miner. Pet*. **67**,
723 417–431.
724 Dunn R. A., Toomey D. R. and Solomon S. C. (2000) Three-dimensional seismic
725 structure and physical properites of the crust and shallow mantle beneath the East
726 Pacific Rise at 9°30'N. *J. Geophys. Res.* **105**, 23,523–537,555.
727 Gale A., Dalton C. A., Langmuir C. H., Su Y. and Schilling J. G. (2013) The mean
728 composition of ocean ridge basalts. *Geochemistry, Geophysics Geosystems* **14**, 489–
729 518.
730 Gao, Y., Hoefs, J., Hellebrand, E., von der Handt, A. and Snow, J.E., (2007). Trace
731 element zoning in pyroxene from ODP Hole 735B gabbros: diffusive exchange or
732 synkinematic crystal fractionation. *Contrib. to Miner. Pet*. **153**, 429–442.

733 Gillis K. M., Snow J. E., Klaus A., Abe N., Adriao A. B., Akizawa N., Ceuleneer G.,
734 Cheadle M. J., Faak K., Falloon T. J., Friedman S. A., Godard M., Guerin G.,
735 Harigane Y., Horst A. J., Hoshide T., Ildefonse B., Jean M. M., John B. E., Koepke
736 J., Machi S., Maeda J., Marks N. E., McCaig A. M., Meyer R., Morris A., Nozaka
737 T., Python M., Saha A. and Wintsch R. P. (2014) Primitive layered gabbros from
738 fast-spreading lower oceanic crust. *Nature* **505**, 204–207.
739 Hekinian, R., Hébert, R., Maury, R.C. and Berger, E.T., (1985). Orthopyroxene-bearing
740 gabbroic xenoliths in basalts from the East Pacific Rise axis near 12°50'N. *Bull.*
741 *Miner*. **108**, 691–698.
742 Hekinian, R. and Walker, R., (1987). Diversity and spatial zonation of volcanic rocks
743 from the East Pacific Rise near 21°N. *Contrib. Miner. Pet*. **96**, 265–280.
744 Huppert H. E. and Sparks R. S. J. (1980) The fluid dynamics of a basaltic magma
745 chamber replenished by influx of hot, dense ultrabasic magma. *Contrib. Miner. Pet.*
746 **75**, 279–289.
747 Jackson M. G. and Carlson R. W. (2012) Homogeneous superchondritic $^{142}Nd/^{144}Nd$ in
748 the mid-ocean ridge basalt and ocean island basalt mantle. *Geochemistry, Geophys.*
749 *Geosystems* **13**. Doi:10.1029/2012GC004114
750 Jenner, F.E. and O'Neill, H., St. C., (2012). Analysis of 60 elements in 616 ocean floor
751 basaltic glasses. *Geochem. Geophys. Geosyst*. **13**. doi:10.1029/2011GC004009
752 John, B.E., Foster, D.A., Murphy, J.M., Cheadle, M.J., Baines, A.G., Fanning, C.M. and
753 Copeland, P., (2004). Determing the cooling history of in situ lower oceanic crust -
754 Atlantis Bank, SW Indian Ridge. *Earth Planet. Sci. Lett*. **222**, 145–160.

755 Kent, G.M., Harding, A.J. and Orcutt, J.A., (1993). Distribution of magma beneath the
756 East Pacific Rise between the Clipperton Transform and the 9°17'N deval from
757 forward modeling of common depth point data. *J. Geophys. Res.* **98**, 13,913–
758 945,969.
759 Langmuir, C.H., (1989). Geochemical consequences of in situ differentiation. *Nature*
760 340, 199–205.
761 Langmuir C. H., Klein E. M. and Plank T. (1992) Petrological Systematics of Mid-Ocean
762 Ridge Basalts: Constraints on Melt Generation Beneath Ocean Ridges. In *Mantle*
763 *flow and melt generation at Mid-Ocean Ridges* (eds. J. Phipps Morgan, G. K.
764 Blackman, and J. M. Sinton). AGU Monograph 71, p. 183-280.
765 Lissenberg, C.J., MacLeod, C.J., Howard, K.A. and Godard, M., (2013). Pervasive
766 reactive melt migration through fast-spreading lower oceanic crust (Hess Deep,
767 equatorial Pacific Ocean). *Earth Planet. Sci. Lett*. **361**, 436-447.
768 Liu, L. and Lowell, R.P., (2009). Models of hydrothermal heat output from a convecting,
769 crystallizing, replenished magma chamber beneath an oceanic spreading center. *J.*
770 *Geophys. Res.* **114**. Doi:10.1029/2011GC004009
771 Michael, P.J. and Cornell, W.C., (1998). Influence of spreading rate and magma supply
772 on crystallization and assimilation beneath mid-ocean ridges: evidence from chlorine
773 and major element chemistry of mid-ocean ridge basalts. *J. Geophys. Res*. **103**,
774 18325–18356.
775 Michael, P.J. and Schilling, J.-G., (1989). Chlorine in mid-ocean ridge magmas: Evidence
776 for assimilation of seawater-influenced components. *Geochim. Cosmochim. Acta* **53**,
777 3131–3143.

778 Moore A., Coogan L. A., Costa F. and Perfit M. R. (2014) Primitive melt replenishment
779 and crystal-mush disaggregation in the weeks preceding the 2005–2006 eruption
780 9◦50′N, EPR. *Earth Planet. Sci. Lett.* **403**, 15–26.
781 Nielsen R. L. (1988) A model of the simulation of combined major and trace element
782 liquid lines of descent. *Geochim. Cosmochim. Acta* **52**, 27–38.
783 Nielsen R. L. (1990) Simulation of igneous differentiation processes. *Rev. Mineral.*
784 *Geochemistry* **24** , 65–105.
785 Nielsen, R.L. and DeLong, S.E., (1992). A numerical approach to boundary layer
786 fractionation: application to differentiation in natural systems. *Contrib. Miner. Pet*.
787 **10**, 355–369.
788 O'Hara, M.J., (1968). Are ocean floor basalts primary magma? *Nature* **220**, 683–685.
789 O'Hara, M.J., (1977). Geochemical evolution during fractional crystallization of a
790 periodically refilled magma chamber. *Nature* **266**, 503–507.
791 O'Hara, M.J. and Fry, N., (1996a). The Highly Compatible Trace Element Paradox -
792 Fractional Crystallisation Revisited. *Jour. Pet*. **37**, 859–890.
793 O'Hara, M.J. and Fry, N., (1996b). Geochemical Effects of Small Packet Crystallisation
794 in Large Magma Chambers - Further resolution of the Highly Compatible Element
795 Paradox. *Jour. Pet*. **37**, 891–925.
796 O'Hara, M.J. and Herzberg, C., (2002). Field relations, petrology, major element data and
797 phase equilibria in basalt petrogenesis: in praise of the Buffalo's carcass. *Geochim.*
798 *Cosmochim. Acta* **66**, 2167–2191.
799 O'Neill, H. St C. and Jenner, F.E., (2012). The global pattern of trace-element
800 distributions in ocean floor basalts. *Nature* **491**, 698–704.

801 Pan, Y. and Batiza, R., (2002). Mid-ocean ridge magma chamber processes: constraints
802 from olivine zonation in lavas from the East Pacific Rise at 9°30'N and 10°30'N. *J.*
803 *Geophys. Res.* **107**; 200210.1029/2001JB000435.
804 Pan, Y. and Batiza, R., (2003). Magmatic processes under mid-ocean ridges: a detailed
805 mineralogical study of lavas from the East Pacific Rise 9°30'N, 10°30'N and
806 11°20'N. *Geochem. Geophys. Geosys*. 4**,** doi:10.1029/2002GC000309.
807 Perfit M. R., Fornari D. J., Malahoff A. and Embley R. W. (1983) Geochemical Studies
808 of Abyssal Lavas Recovered by DSRV Alvin From Eastern Galapagos Rift, Inca
809 Transform, and Ecuador Rift 3: Trace element abundnces and petrogenesis. *J.*
810 *Geophys. Res*. **88**, 10551–10572.
811 Perk, N.W., Coogan, L.A., Karson, J.A., Klein, E.M. and Hanna, H., (2007). Primitive
812 cumulates from the upper crust formed at the East Pacific Rise. *Contrib. to Miner.*
813 *Petrol.* **154**, 575–590.
814 Phipps Morgan, J. and Chen, Y.J., (1993). The Genesis of oceanic crust - magma
815 injection, hydrothermal cooling, and crustal flow. *Jour. Geophys. Res.* **98**, 6283–
816 6297.
817 Pollock M. A., Klein E. M., Karson J. A. and Coleman D. S. (2009) Compositions of
818 dikes and lavas from the Pito Deep Rift: Implications for crustal accretion at
819 superfast spreading centers. *J. Geophys. Res. Earth* **114**,
820 doi:10.1029/2007JB005436.
821 Rhodes, J.M., Dungan, M.A., Blanchard, D.P. and Long, P.E., (1979). Magma mixing at
822 mid-ocean ridges: evidence from basalts drilled near 22°N on the Mid-Atlantic
823 Ridge. *Tectonophysics* 55, 35–61.

824 Ridley I., Perfit M. R., Smith M. C. and Fornari D. J. (2006) Magmatic processes in
825 developing oceanic crust revealed in a cumulate xenolith collected at the East
826 Pacific Rise, 9°50'N. *Geochemistry Geophys. Geosystems* **7**, doi:
827 10.1029/2006GC001316.
828 Robson, D. and Cann, J. R. (1982). A geochemical model of mid-ocean ridge magma
829 chambers. *Earth and Planetary Science Letters* **60**, 93–104.
830 Ross, K. and Elthon, D., (1997). Cumulus and postcumulus crystallisation in the oceanic
831 crust: Major and trace-element geochemistry of Leg 153 Gabbroic rocks, in: Karson,
832 J.A., Cannat, M., Miller, D.J., Elthon, D. (Eds.), *Proc. Sci. Results ODP Leg 153*.
833 Ocean Drilling Program, College station, Texas, pp. 333–353.
834 Saal, A. E., Hauri, E. H., Langmuir, C. H. and Perfit, M. R. (2002). Vapour
835 undersaturation in primitive mid-ocean-ridge basalt and the volatile content of
836 Earth's upper mantle. *Nature* **419**, 451–455.
837 Sims, K. W. W., Goldstein, S. J. and 12 others (2002). Chemical and isotopic constraints
838 on the generation and transport of magma beneath the East Pacific Rise. *Geochim.*
839 *Cosmochim. Acta.* **66**, 3481–3504.
840 Singh, S.C., Kent, G.M., Collier, J.S., Harding, A.J. and Orcutt, J.A., (1998). Melt to
841 mush variations in crustal magma chamber properties along the ridge crest at the
842 southern East Pacific Rise. *Nature* **394**, 874–878.
843 Sinton, J. M. and Detrick, R. S. (1992). Mid-Ocean Ridge Magma Chambers. *J. Geophys.*
844 *Res.* **97**, 197–216.
845 Stewart, M. A., Klein, E. M. and Karson, J. A. (2002). Geochemistry of dikes and lavas
846 from the north wall of th Hess Deep Rift: insights into the four-dimensional

847 character of crustal construction at fast spreading mid-ocean ridges. *J. Geophys. Res.*
848 **107**, DOI 10.1029/2001JB000545.
849 Van Orman, J.A., Grove, T.L. and Shimizu, N., (2001). Rare earth element diffusion in
850 diopside: influence of temperature, pressure, and ionic radius and an elastic model
851 for diffusion in silicates. *Contrib. Miner. Pet*. **141**, 687–703.
852 Villiger, S., Muntener, O. and Ulmer, P. (2007). Crystallization pressures of mid-ocean
853 ridge from major element variations of glasses from and fractional crystallization
854 experiments. *Journal of Geophysical Research* **112**, doi:10.1029/2006JB004342.
855 White W. M. and Bryan W. B. (1977) Sr-isotope, K, Rb, Cs, Sr, Ba, and rare-earth
856 geochemistry of basalts from the FAMOUS area. *Geol. Soc. Am. Bull.* **88**, 571–576.
857 Wood, B.J. and Blundy, J. (2003). Trace Element Partitioning under Crustal and
858 Uppermost Mantle Conditions: The Influences of Ionic Radius, Cation Charge,
859 Pressure, and Temperature, in: *Treatise on Geochemistry, Volume 3*: Carlson, R.W.
860 (Ed.), The Mantle and Core. Elsevier-Pergamon, Oxford, pp. 395–424.
861 Workman, R. K. and Hart, S. R. (2005). Major and trace element composition of the
862 depleted MORB mantle (DMM). *Earth and Planetary Science Letters* **231**, 53–72.
863

FIGURE CAPTIONS:

Figure 1. Features of MORB inconsistent with fractional crystallization being the sole differentiation mechanism: (a) over-enrichment of incompatible elements (here shown as Th) with respect to that predicted by fractional crystallization shown for an isotopically homogeneous suite of MORB from the East Pacific Rise (Regelous et al., 1999) and the MORB dataset of Jenner and O'Neill (2012 excluding seamounts, aseismic ridges and back arc basins; inset). Fractional crystallization is shown by the solid lines with Kd_{Th} set to zero and Kd_{Mg} as labeled on the main figure; (b) under-depletion of compatible elements (here shown as Ni from the global MORB glass dataset of Jenner and O'Neill (2012; excluding seamounts, aseismic ridges and back arc basins) with respect to a fractional crystallization model. The fractional crystallization model (solid grey line) was derived by Petrolog modelling of the bulk crustal composition of Gillis et al. (2014) with a temperature and composition dependent $kd^{Ni}_{olivine}$ calculated following Li and Ripley (2010) with $kd^{Ni}_{clinopyroxer}$ set to 0.3 $kd^{Ni}_{olivine}$ and $kd^{Ni}_{plagioclase}$ = 0. The initial melt Ni content is 350 ppm, in equilibrium with mantle-like olivine containing 2700 ppm Ni. The dashed grey line connects the parental melt and the most evolved glass demonstrating that most samples could be produced by mixing evolved and primitive melts; (c) variation in CaO/Al_2O_3 with MgO in the Smithsonian MORB glass database (filtered to

886 K_2O/TiO_2<0.15 to exclude T- and E-MORB) and averages of these data binned in
887 decreasing MgO content at every 11 samples (black symbols) and every 0.5 wt% MgO
888 (large open symbols). Troctolite crystallization drives CaO/Al_2O_3 up and gabbro
889 fractionation drives CaO/Al_2O_3 down, as shown in the Petrolog model (solid grey line
890 calculated as for part b). The data show little or no evidence of any change from
891 clinopyroxene-free to clinopyroxene-bearing cumulates with decreasing MgO. This is
892 supported by least-squares modeling of the cumulate mode required to drive the average
893 melt composition to lower MgO contents shown as histograms (labeled by the range of
894 MgO content the crystal extract was calculated over); and (d) comparison of the
895 composition of olivine 'phenocrysts' in MORB and their host glass ("spreading center"
896 data downloaded from PetDB June 2014; 2127 olivine-glass pairs). Lines show
897 equilibrium compositions for three different exchange coefficients (0.27, 0.30, 0.33);
898 most olivine are too magnesium-rich to be in equilibrium with their host. Due to rapid
899 diffusion of Mg and Fe in olivine this disequilibrium requires mixing within years of
900 eruption and suggests that mixing of an olivine-poor evolved magma with an olivine
901 bearing primitive magma is common.
902
903 Figure 2. Results of modeling RMTX magma chambers: (a) relative mass fractions of the
904 maximum magma chamber mass tapped and crystallized per cycle of replenishment to
905 achieve a given steady-state erupted melt MgO content using the equations of O'Hara and
906 Herzberg (2002; Note that the definitions of their properties C_D and C_E are inverted in
907 their appendix but the equations are correct). Following O'Neill and Jenner (2012) this is
908 calculated assuming a perfectly incompatible element ($X_{kd=0}$) has a slope on a plot of

MgO v Log($X_{kd=0}$) of -0.26 and the parental melt has a MgO content of 10 wt%; (b) result of simulation of RMTX magma chamber using Petrolog (Danyushevsky and Plechov, 2011) iterated manually for three different sets of values of the mass fractions tapped and crystallized per cycle (see key in part c). K_2O behaves perfectly incompatible in this modeling. The labels on the tops of the Petrolog models are the steady-state values (MgO / K_2O both in wt%) determined using the analytical solution for constant partition coefficients (kd^{bulk}_{MgO} = 1.9; $kd^{bulk}_{K_2O}$ = 0). This is identical to the Petrolog solution for K_2O as this has a partition coefficient of zero throughout but is somewhat different for MgO. The model MgO content was changing by <0.015 wt% when the modeling was stopped (suggesting a close approach to the steady-state value) but the steady state K_2O content was not reached in any case as this takes many cycles (O'Hara, 1977). The inset shows a numerical solution for the constant partition coefficient model (4% tapped, 16% crystallized) showing the large number of cycles (labeled) required to reach the steady-state composition; (c) result of simulation of RMTX magma chamber using Petrolog (Danyushevsky and Plechov, 2011) for MgO-CaO showing the different steady-state melt compositions and the different pathways followed to reach the steady-state for different mass fractions tapped and crystallized per cycle. These could be misinterpreted as indicating different pressures of crystallization. For example, the labels show the pressures of crystallization calculated for the steady-state compositions using the approach of Villiger et al. (2007). Petrolog models used the same starting composition as O'Neill and Jenner (2012), a crystallization pressure of 1 kbar, oxygen fugacity buffered at QMF, and the crystal-melt exchange models of Langmuir et al. (1992) for olivine, plagioclase and clinopyroxene and of Beattie (1993) for orthopyroxene. Models were

iterated manually to simulate a RMTX chamber undergoing perfect fractional crystallization.

Figure 3: Examples of the behaviour of incompatible trace elements in clinopyroxene and plagioclase in oceanic gabbros: (a) strong zoning of 100xLa, Y and Zr/Nd in the best-studied clinopyroxene crystal ($Mg\#_{79-85}$) from Coogan et al. (2000b) in a coarse grained gabbro from the MARK area of the Mid-Atlantic Ridge. The inset shows that although the Zr/Nd ratio of the clinopyroxene increases by about an order of magnitude from core-to-rim there is no change in this ratio in MORB during differentiation (data from global compilation of Gale et al., 2013); (b) zoning of La and Y in the plagioclase crystal (An_{57-60}) adjacent to the clinopyroxene shown in part a. Note the lack of enrichment in Y at the plagioclase rim in contrast to clinopyroxene; (c) ratio of rim-to-core concentrations of La and Y in plagioclase crystals in plutonic rocks from the MARK area (Coogan et al., 2000b) and Hess Deep (Lissenberg et al., 2013). Plagioclase rims are enriched in La relative to their cores but are generally depleted in Y consistent with diffusive loss of Y from plagioclase to clinopyroxene during cooling. Samples of the shallowest gabbros from Hess Deep, that would have cooled the fastest (and hence undergone the least diffusive exchange), have higher Y in plagioclase rims than cores.

Figure 4. Models of zoning in adjacent clinopyroxene (left column) and plagioclase (right column) produced by fractional crystallization (initial profiles) and then subsequent subsolidus diffusive relaxation at two different cooling rates (note different scales for different phases). Details of the modeling are given in the text. (a, b) La; (c, d) Nd; (e, f)

955 Yb. The inset in part c shows the ratio of the initial Nd concentration (Nd_{ini}) to the final
956 Nd concentration with the former used as a proxy for the Zr concentration as discussed in
957 the text. The large increase in Nd_{ini}/Nd in the clinopyroxene rim in the model mimics the
958 large increase in Zr/Nd observed in clinopyroxene in oceanic gabbros that has previously
959 been interpreted as reflecting growth from melts with highly fractionated Zr/Nd ratios
960 (Fig. 3a). Plagioclase Y zoning can invert from showing high Y rims after crystallization
961 to low Y rims after diffusive exchange with clinopyroxene. This provides a simple
962 explanation for low Y rims in plagioclase in oceanic gabbros (e.g. Fig. 3c). Concentration
963 units are arbitrary.
964
965 Figure 5. Comparison of the observed (O'Neill and Jenner, 2012) and modeled slopes of
966 plots of Log[*X*] versus MgO for the closed system *in situ* crystallization model of
967 Langmuir (1989) and an open system *in situ* crystallization model (O'Hara and Fry,
968 1996b; O'Hara and Herzberg, 2002). The closed system model assumes equilibrium
969 crystallization in the mush zone until 40% melt remains followed by return of this
970 interstitial melt to the eruptible reservoir. The slope was calculated from synthetic data
971 generated for various values of F and f_a. The open system model of O'Hara and Fry
972 (1996b) gives a steady-state (i.e., fixed) composition. To allow comparison to the data a
973 numerical approach was used in which the mass fractions tapped (0.04) and crystallized
974 (0.16) are held constant but the mass fraction of replenishment was drawn from a
975 Gaussian distribution about the steady-state value of 0.2 (±0.05 1σ). Both models use the
976 partition coefficients of O'Neill and Jenner (2012) for ease of comparison to their results.
977 No attempt was made to optimize either model to fit the data.

978

979 Figure 6. Comparison of the results of a numerical RMTX model, in which crystallization
980 occurs *in situ*, and the composition of a suite of lavas and dikes from Hess Deep (Stewart
981 et al., 2002) for: (a) MgO-TiO_2 and (b) MgO-Nb. One thousand synthetic data points are
982 shown. A mass fraction of 0.2±0.07 (1σ, with the distribution truncated to avoid negative
983 values) of the chamber was replenished per cycle and the mass fractions erupted (0.04)
984 and crystallized (0.16) were held constant. The slightly higher standard deviation on the
985 mass fraction replenished used in this modeling than that shown in Fig. 5 was found to
986 produce a visually better fit to the data. The slopes of MgO v Log[*X*] for the data and
987 model compare well for both TiO_2 (-0.11 v -0.10) and Nb (-0.19 v -0.17). The inset in
988 part a shows small sub-sets of the model results produced over 10-20 consecutive cycles
989 with mass fractions of replenishment that are below average (path 1), average (path 2) or
990 above average (path 3; see also Caroff et al., 1997). The solid line depicts fractional
991 crystallization. Co = parental melt composition.

Figure 1

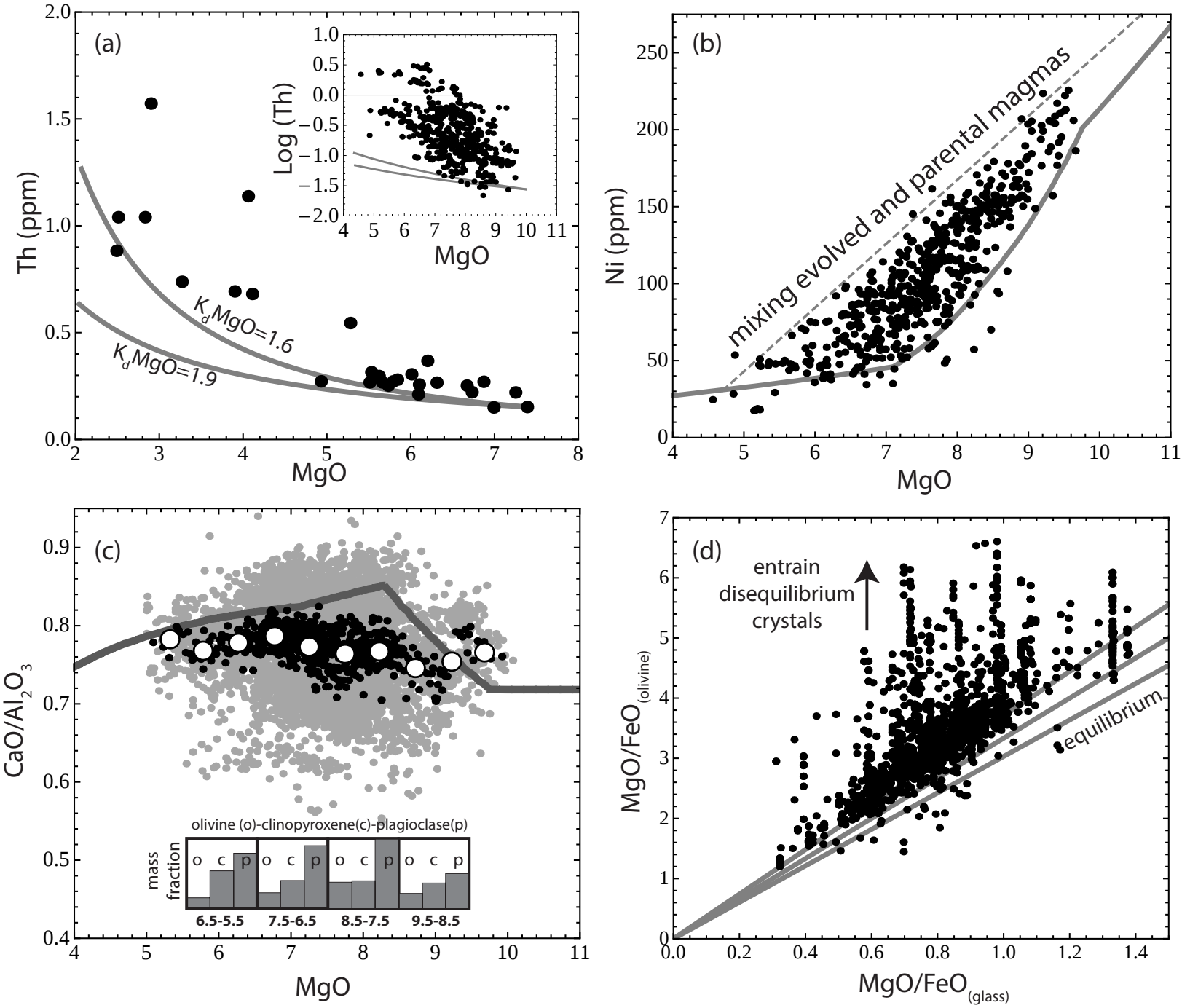
(a)
Th (ppm)
MgO
Log (Th)
MgO
K_dMgO=1.6
K_dMgO=1.9
(b)
Ni (ppm)
MgO
mixing evolved and parental magmas
(c)
CaO/Al$_2$O$_3$
MgO
olivine (o)-clinopyroxene(c)-plagioclase(p)
mass fraction
o c p o c p o c p o c p
6.5-5.5
7.5-6.5
8.5-7.5
9.5-8.5
(d)
MgO/FeO$_{(olivine)}$
MgO/FeO$_{(glass)}$
entrain disequilibrium crystals
equilibrium

Figure 2

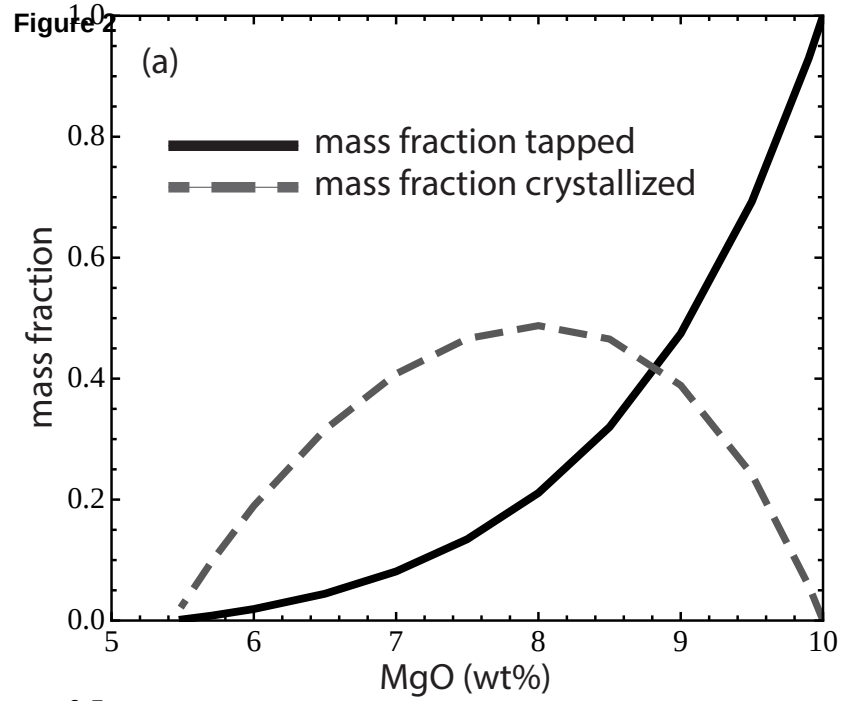
(a)
mass fraction tapped
mass fraction crystallized
mass fraction
MgO (wt%)

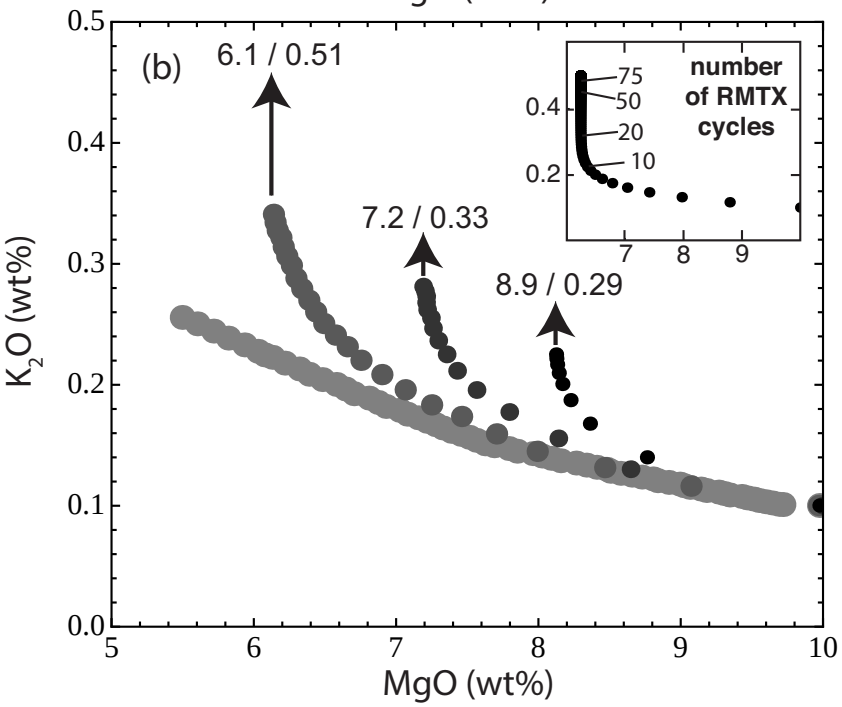
(b)
6.1 / 0.51
7.2 / 0.33
8.9 / 0.29
number of RMTX cycles
75
50
20
10
K2O (wt%)
MgO (wt%)

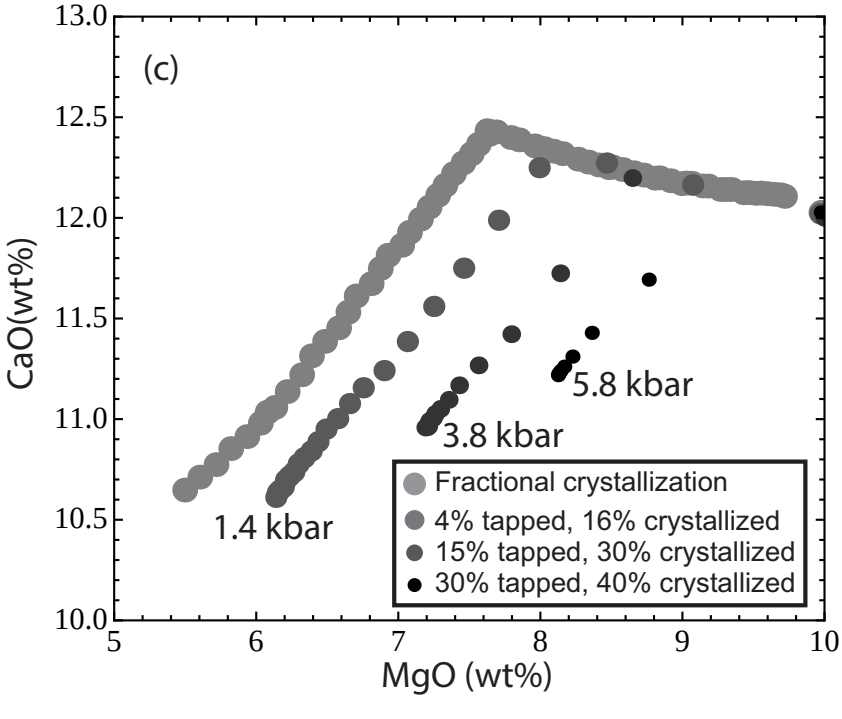
(c)
5.8 kbar
3.8 kbar
1.4 kbar
Fractional crystallization
4% tapped, 16% crystallized
15% tapped, 30% crystallized
30% tapped, 40% crystallized
CaO(wt%)
MgO (wt%)

Figure 3

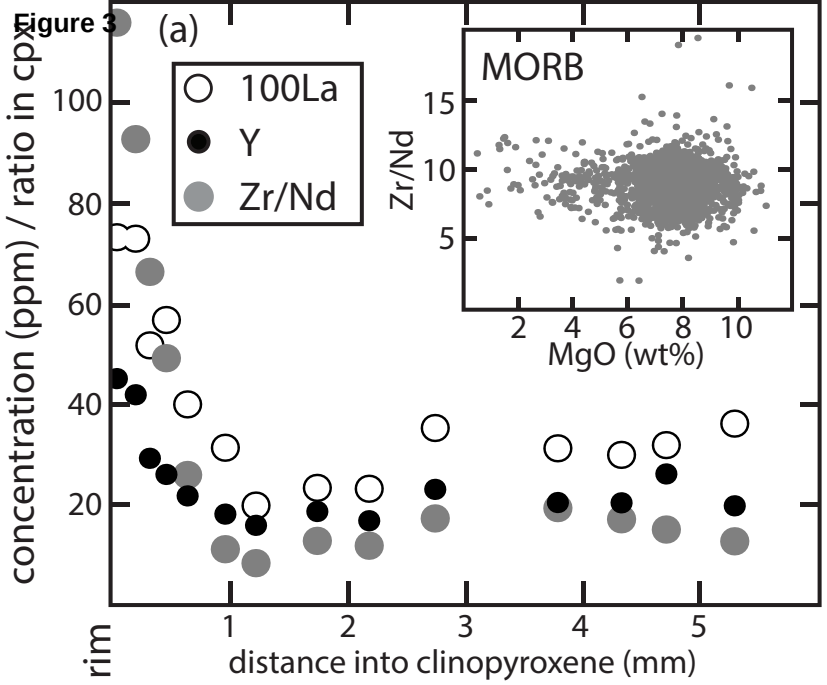
(a)
100La
Y
Zr/Nd
MORB
Zr/Nd
MgO (wt%)
concentration (ppm) / ratio in cpx
rim
distance into clinopyroxene (mm)

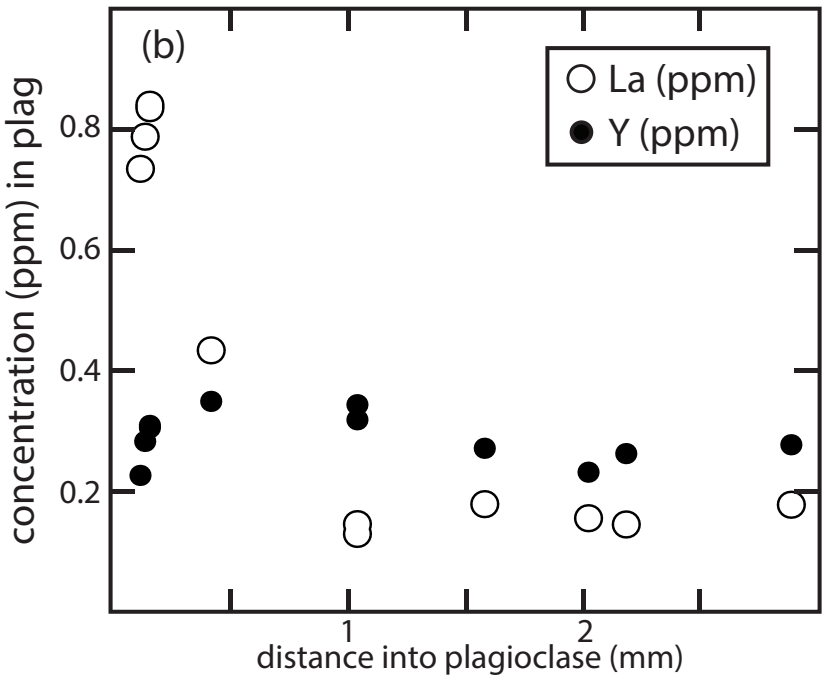
(b)
La (ppm)
Y (ppm)
concentration (ppm) in plag
distance into plagioclase (mm)

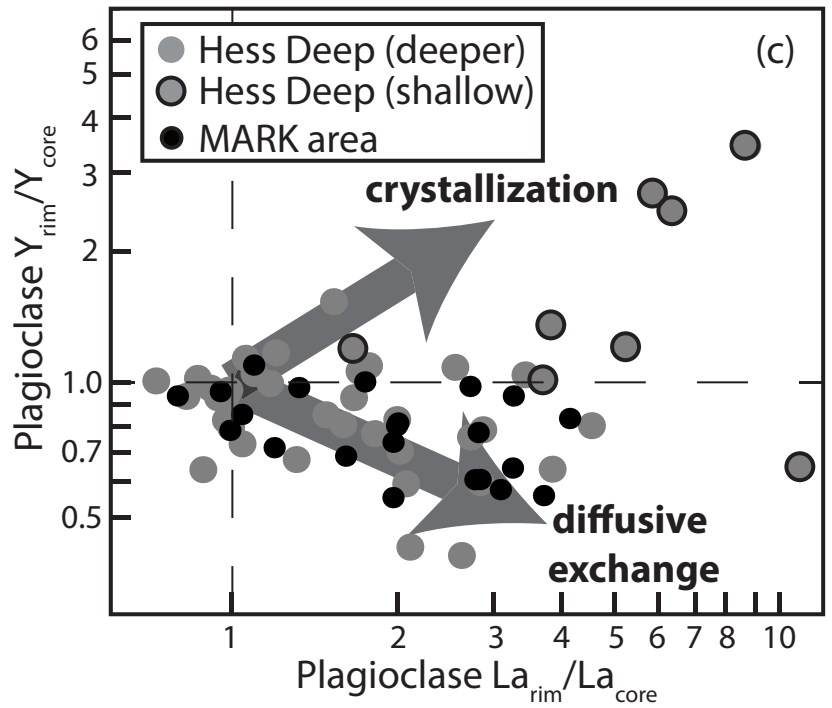
(c)
Hess Deep (deeper)
Hess Deep (shallow)
MARK area
crystallization
diffusive
exchange
Plagioclase Y_rim/Y_core
Plagioclase La_rim/La_core

Figure 4

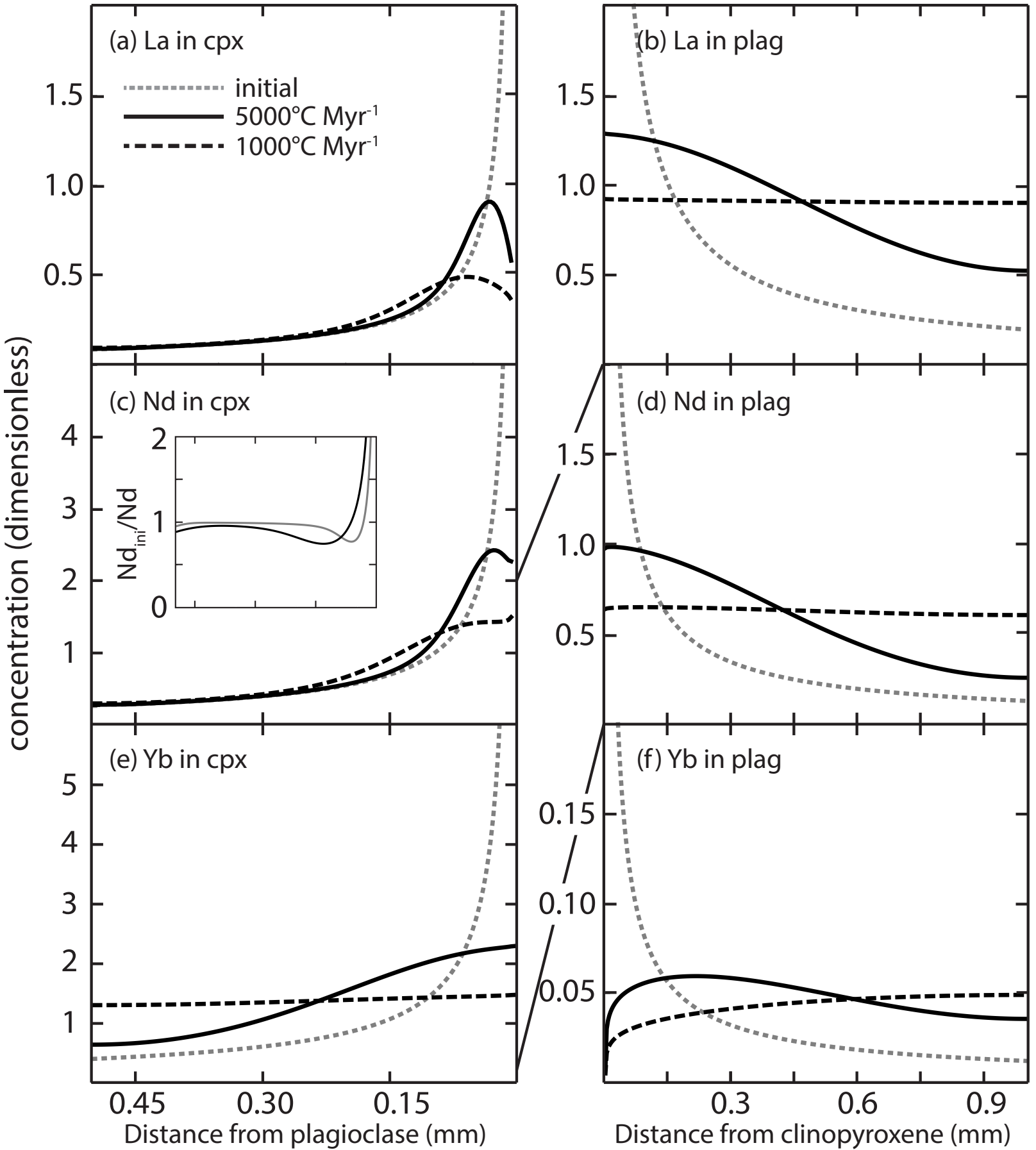
(a) La in cpx
initial
5000°C Myr-1
1000°C Myr-1
(b) La in plag
(c) Nd in cpx
Ndini/Nd
(d) Nd in plag
(e) Yb in cpx
(f) Yb in plag
concentration (dimensionless)
Distance from plagioclase (mm)
Distance from clinopyroxene (mm)

Figure 5

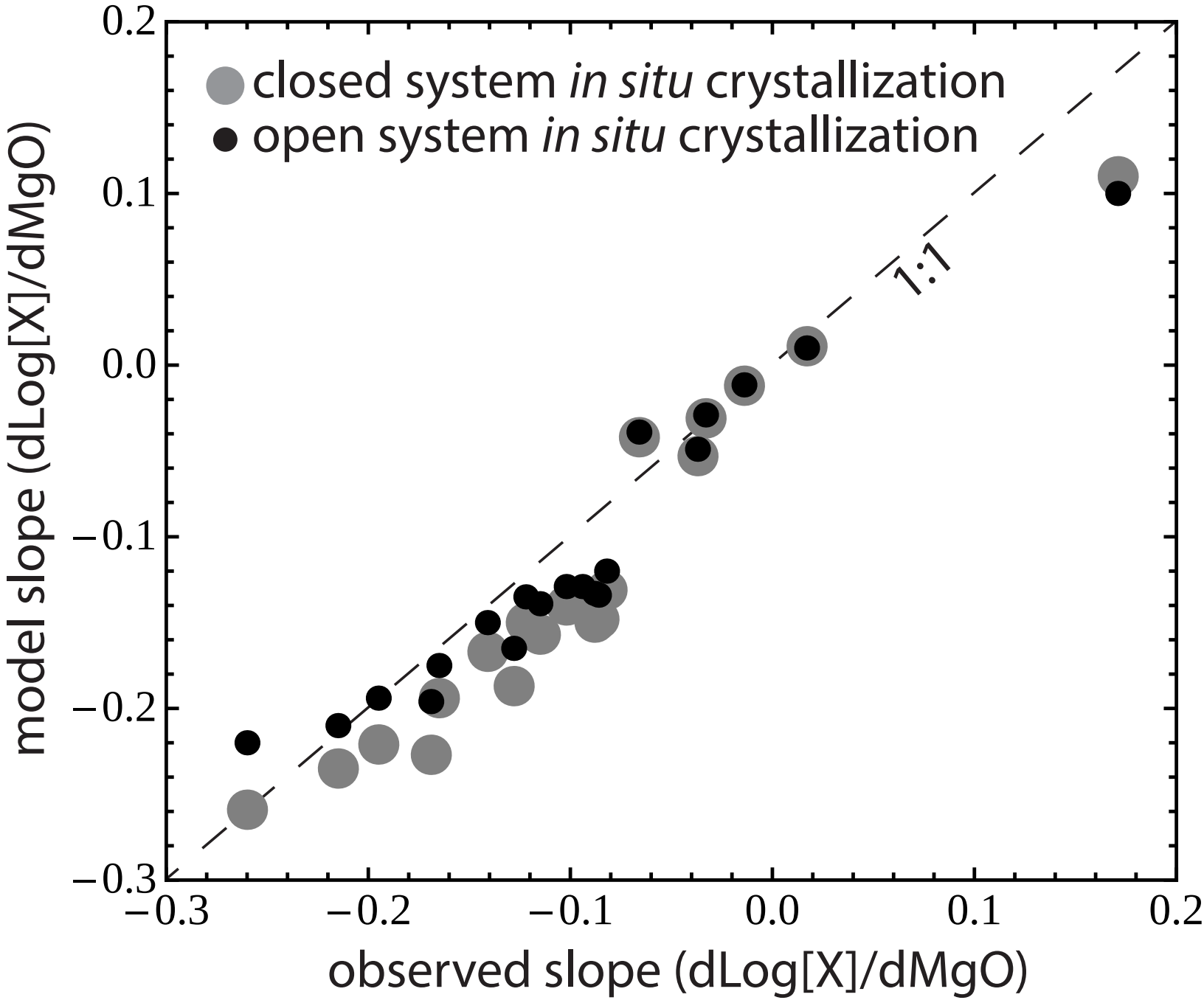
closed system *in situ* crystallization
open system *in situ* crystallization
1:1
model slope (dLog[X]/dMgO)
observed slope (dLog[X]/dMgO)
0.2
0.1
0.0
−0.1
−0.2
−0.3
−0.3
−0.2
−0.1
0.0
0.1
0.2

Figure 6

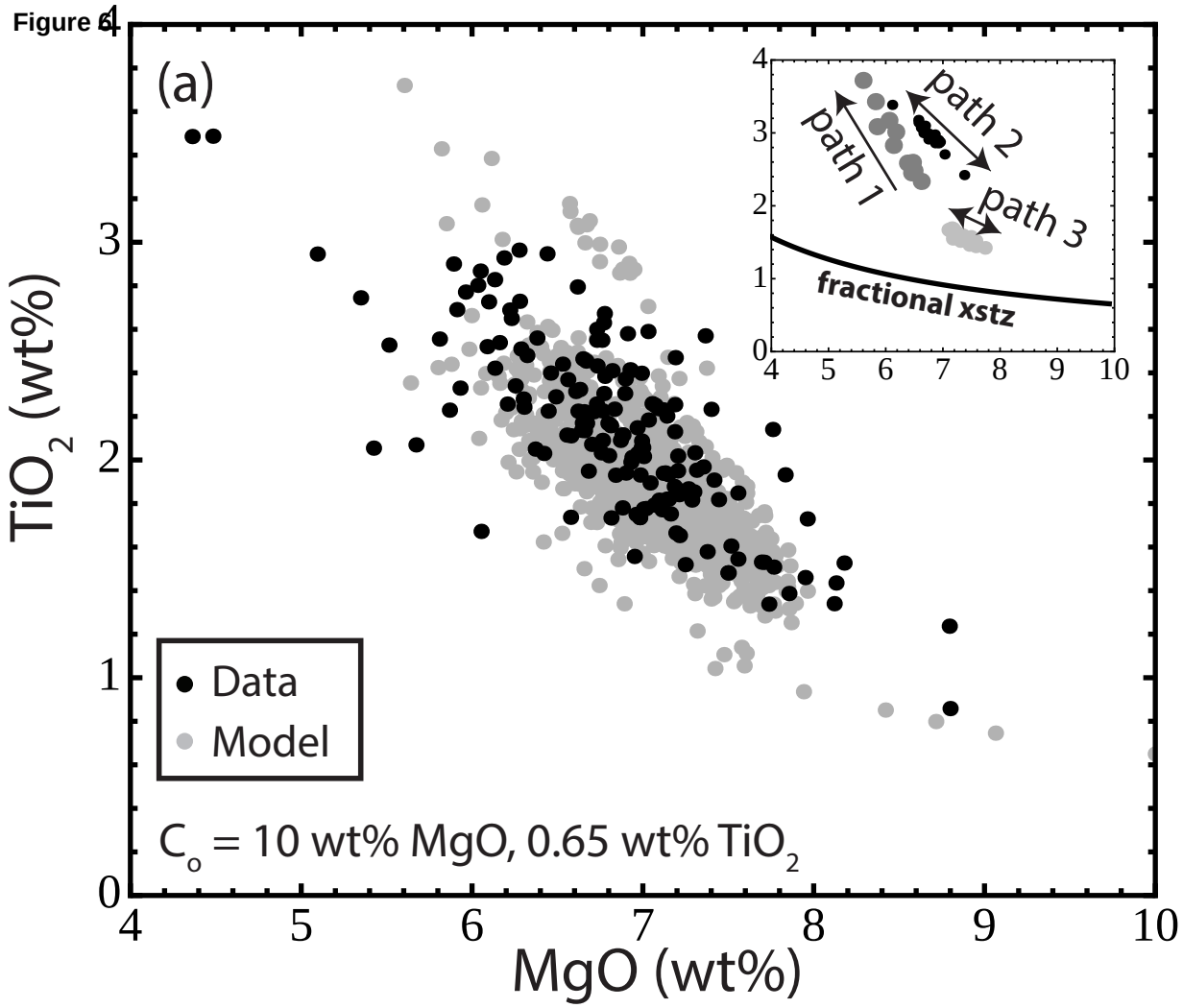
(a)
TiO2 (wt%)
MgO (wt%)
Data
Model
C_o = 10 wt% MgO, 0.65 wt% TiO2
path 1
path 2
path 3
fractional xstz

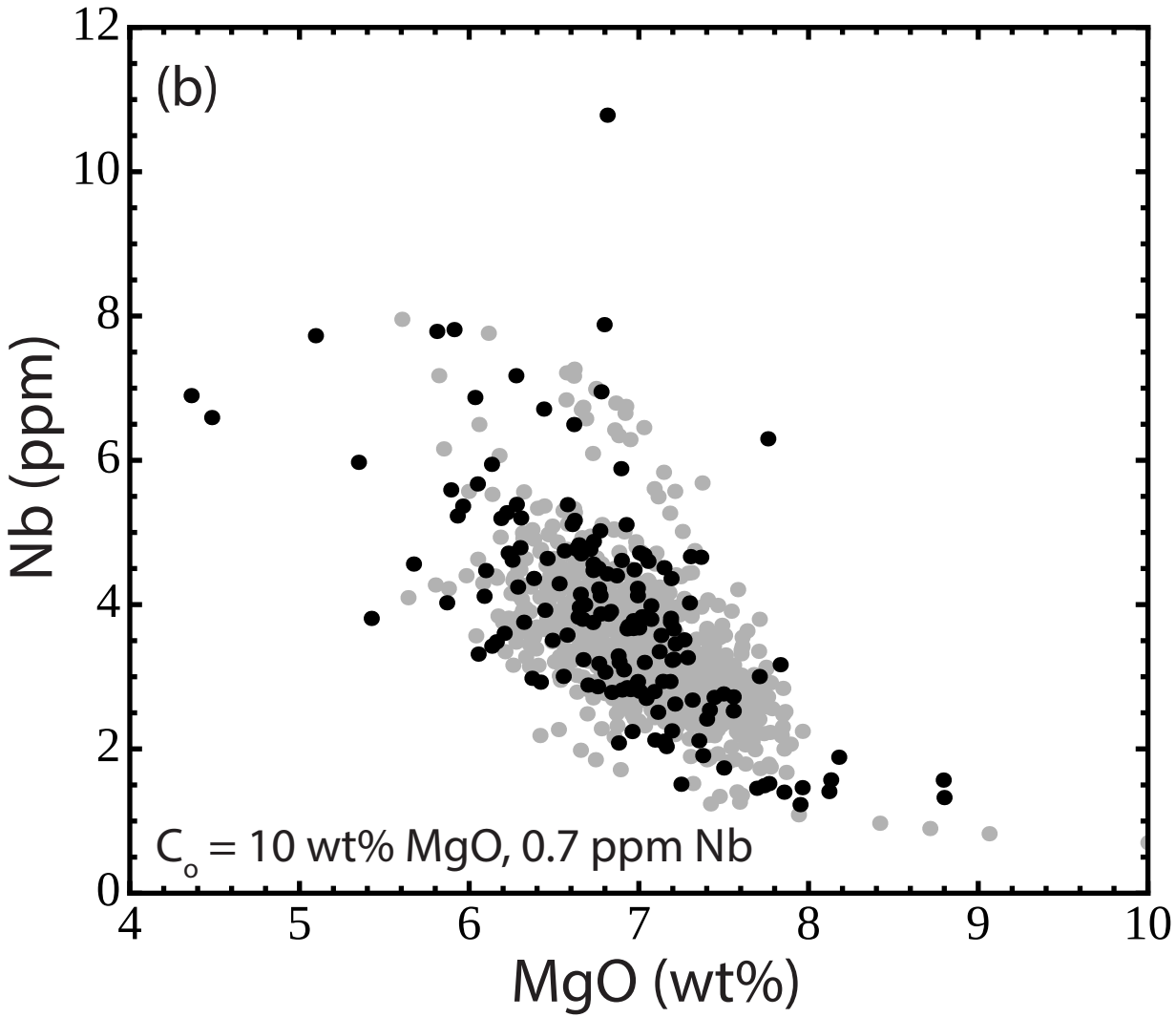
(b)
Nb (ppm)
MgO (wt%)
C_o = 10 wt% MgO, 0.7 ppm Nb